

**Timescales of Southern Ocean Eddy Equilibration**

Anirban Sinha\* and Ryan P. Abernathey†

*Columbia University, New York, NY 10027.*

\*Corresponding author address: Applied Physics and Applied Mathematics Department, Columbia University, NY 10027.

E-mail: as4479@columbia.edu

†Department of Earth and Environmental Sciences, Columbia University, NY 10027.

## ABSTRACT

Stratification in the Southern Ocean (SO) is determined by a competition primarily between westerly wind driven upwelling and baroclinic eddy transport. We investigate the timescales of mesoscale eddy equilibration in the SO in response to changing winds through an idealized channel model. An analytical framework describing the energetic pathways between wind input, available potential energy (APE), eddy kinetic energy (EKE), and dissipation, provides a simple theory of the phase and amplitude response to oscillating wind stress. The transient ocean response to variable winds lies between the two limits of Ekman response (high frequency limit), characterized by the isopycnal slope responding directly to wind stress, and “eddy saturation” (low frequency limit), wherein all of the anomalous wind work goes into mesoscale eddies. Motivated by an analogy with electric circuits, the systems frequency response is characterized by a complex transfer function: the “eddy filter”. Both the phase and amplitude response of EKE and APE, predicted by the linear analytic framework are verified using multiple ensemble experiments in a high-resolution isopycnal layered coordinate model (GOLD). The results from the numerical experiments show agreement with the linear theory and can be used to explain certain features observed in previous modeling studies of eddy saturation. The implications of these results for baroclinic instability, eddy mixing and transport in the Southern ocean are discussed.

<sup>28</sup> **1. Introduction**

<sup>29</sup> On account of the Southern Ocean's (SO's) unique geometry, the Antarctic Circumpolar Current  
<sup>30</sup> (ACC) is, compared to other regions, a dynamically unique ocean current, with large zonal trans-  
<sup>31</sup> port and deep stratification (Rintoul and Naveira-Garabato 2013). In the contemporary theory,  
<sup>32</sup> (Johnson and Bryden 1989; Marshall and Radko 2003; Abernathey and Cessi 2014), the steady  
<sup>33</sup> state equilibrium for ACC stratification and overturning circulation is determined by a competi-  
<sup>34</sup> tion between buoyancy transport by wind driven upwelling and baroclinic eddy transport. Strong  
<sup>35</sup> westerly winds over the latitude belt between 50° S and 55° S steepen the meridional isopycnal  
<sup>36</sup> slopes in the SO through Ekman upwelling, which causes baroclinic instability and leads to baro-  
<sup>37</sup> clinic eddies. These eddies transport heat and momentum, flattening the isopycnal slope. The  
<sup>38</sup> equilibrium energy balance is primarily between available potential energy (APE) caused due to  
<sup>39</sup> increased isopycnal slopes and eddy kinetic energy (EKE), due to the resulting baroclinic eddies.  
<sup>40</sup> The sensitivity of the isopycnal slope and the associated thermal wind transport to the wind forcing  
<sup>41</sup> has been studied extensively through many eddy-permitting and eddy-resolving models (Hallberg  
<sup>42</sup> and Gnanadesikan 2001; Henning and Vallis 2005; Hallberg and Gnanadesikan 2006; Meredith  
<sup>43</sup> and Hogg 2006; Hogg et al. 2008; Viebahn and Eden 2010; Farneti and Delworth 2010; Treguier  
<sup>44</sup> et al. 2010; Abernathey et al. 2011; Meredith et al. 2012; Morrison and Hogg 2013; Munday et al.  
<sup>45</sup> 2013; Abernathey and Cessi 2014; Pennel and Kamenkovich 2014; Hogg et al. 2015; Munday and  
<sup>46</sup> Zhai 2015; Wilson et al. 2015; Marshall et al. 2016). It has also been well established that the  
<sup>47</sup> mesoscale eddies associated with the Southern Ocean play an important role in modulating the  
<sup>48</sup> strength of the Meridional Overturning Circulation (MOC), by contributing an advective “bolus  
<sup>49</sup> transport” (Marshall and Radko 2003; Abernathey et al. 2011). The MOC in  $\sigma$  coordinates is de-  
<sup>50</sup> scribed as the small residual between the eddy-driven overturning circulation and the wind-driven

51 Ekman overturning (Marshall and Radko 2003; Abernathey et al. 2011). While the steady state  
52 theory explains the equilibrium eddy response quite well, it fails to describe the dynamics of the  
53 process of baroclinic equilibration. The full dynamical picture of the time dependent behavior can  
54 be obtained through investigating the transient response.

55 Recent estimates of the ACC transport from observations and models have suggested that there  
56 has been little change in ACC transport over the last 30 years (Cunningham et al. 2003; Hallberg  
57 and Gnanadesikan 2006; Boning et al. 2008; Chidichimo et al. 2014) even though the maximum  
58 zonal wind stress forcing over the SO has increased by at least 20 % during the period 1980 – 2010  
59 (Swart and Fyfe 2012). But this is very difficult to confirm since the observational transport  
60 estimates have errors of at least several sverdrups.

61 From analyzing satellite altimeter data, it was revealed (Meredith and Hogg 2006) that the EKE  
62 exhibits anomalously high values in the ACC around 2-3 years after a peak in eastward wind stress  
63 (quantified by the Southern Annular Mode; SAM). However due to the short length of existing  
64 satellite records, and due to the lack of any direct measurements of MOC in the SO, understanding  
65 the role of time varying patterns in wind stress on the SO dynamics requires the use of numerical  
66 models. The delayed eddy response to wind forcing was investigated with a quasigeostrophic (QG)  
67 eddy-resolving ocean model (Hogg et al. 2003) and it was shown (Meredith and Hogg 2006; Hogg  
68 et al. 2008) that EKE takes 2-3 years to respond to an increase in zonal wind stress (SAM), but once  
69 the adjustment is completed, the EKE becomes linearly proportional to the wind stress magnitude  
70 (Meredith and Hogg 2006; Hogg et al. 2008; Meredith et al. 2012). The authors attributed the lag  
71 to the deep circulation of the ACC and a mechanism was proposed wherein the initial wind energy  
72 is stored as potential energy (PE) and slowly transferred to EKE over several years.

73 Using global eddy-permitting ocean circulation models driven with both idealized and realistic  
74 wind forcing, Langlais et al. (2015) explored the ACC response to interannual wind strengthening

and observed that the response of the barotropic and baroclinic transports and eddy field of the ACC depends on the spatial pattern of the changes in wind forcing. An enhancement of the westerlies over the ACC belt in their numerical model led to an increase of both barotropic and baroclinic transport, with lagged enhancement of the eddy kinetic energy (EKE), while an increase in wind forcing near Antarctica was seen to drive a largely barotropic change in transport with little change in eddy activity.

A recent study by Wilson et al. (2015), with an approach very similar to ours, explored the roles of forced and intrinsic variability in response to a linear increase of wind stress using ensemble runs from a three-layer idealized SO QG model (Hogg et al. 2003) and reported no observed increase in eastward circumpolar volume transport (ACC transport) in response to the increased wind stress. A large part of the time series in ACC transport was explained by a response in which the eddy kinetic energy is linearly proportional to the wind stress with a possible time lag. The energy budget for intrinsic variability at periods shorter than a year was observed to be dominated by exchange between kinetic and potential energy while over longer time scales, the authors found an intrinsic mode, with period around 15 years, which is dominated by changes in potential energy and frictional dissipation (Hogg et al. 2008). An updated analysis of satellite altimetry record (Hogg et al. 2015) revealed that there has been an increase in eddy kinetic energy(EKE) along with a probable decrease in ACC transport. The authors noted two timescales of EKE response to wind stress changes: an interannual response which occurs rapidly, within a couple of years, and an additional slow response with a multidecadal time scales.

Although the role of time-dependent eddy variability in the ACC has been studied previously, using either eddy-resolving QG models (Hogg et al. 2008; Meredith et al. 2012; Wilson et al. 2015), or eddy permitting GCMs with idealized model configurations (Hogg et al. 2015; Langlais et al. 2015), these studies all report that the ACC is “very likely close to an eddy saturated state”

<sup>99</sup> (Hogg et al. 2008). “Eddy saturation” refers to the state where the ACC transport is not signif-  
<sup>100</sup> icantly affected by increased wind stress and instead, the increased winds serve to enhance only  
<sup>101</sup> the eddy strength. This conclusion may possibly be due to the fact that these models either do not  
<sup>102</sup> allow for feedback between the stratification and eddy activity (Hogg et al. 2008; Meredith et al.  
<sup>103</sup> 2012, QG), or do not resolve eddy dynamics (Langlais et al. 2015).

<sup>104</sup> A better understanding of how the Southern Ocean is affected by changing winds requires a  
<sup>105</sup> more mechanistic description of the interactions between mean flow and transient and stationary  
<sup>106</sup> eddies. The first step towards this goal is to characterize the variability in the wind forcing. It was  
<sup>107</sup> shown (Swart and Fyfe 2012) through a comparison of climatologies and trends, in the position and  
<sup>108</sup> strength of the surface westerly wind-stress jet with the Coupled Model Intercomparison Project  
<sup>109</sup> (CMIP) phase 3 and phase 5 models over the historical period from 1979 - 2010 and atmospheric  
<sup>110</sup> reanalyses products, that both the reanalyses and climate models exhibit significant trends (at least  
<sup>111</sup> 20%) in annual mean jet strength. However, in addition to a trend, there exists a clear higher  
<sup>112</sup> frequency variability associated with the wind stress.

<sup>113</sup> To motivate our study, we constructed the timeseries for the jet speed, jet latitude and wind  
<sup>114</sup> stress from the high frequency (6 hourly) Reanalysis (NCEP-NCAR and ERA-Interim) data of  
<sup>115</sup> the surface zonal wind fields over the SO. We also constructed a timeseries for the meridionally  
<sup>116</sup> integrated zonal wind over the latitude belt  $35^{\circ}$  S -  $70^{\circ}$  S (over the SO region). The power spectra  
<sup>117</sup> is then computed from the timeseries in these quantities and plotted in figure 1. Firstly, we observe  
<sup>118</sup> that the there is significantly more power at lower frequencies in comparison to higher frequencies.  
<sup>119</sup> This suggests that the dominant forcing timescale is long. We also see a clear peak around 1/2 year  
<sup>120</sup> period in the power spectra. The fact that the semi-annual peak is also seen in the power spectra  
<sup>121</sup> of the meridionally integrated zonal wind, shows that this is not an artifact of the jet shifting in the  
<sup>122</sup> meridional direction or any discrepancy in the method used for finding the jet. This semi-annual

<sup>123</sup> peak is in fact due to the well known Semi Annual Oscillation that has been observed over SO  
<sup>124</sup> (Taschetto et al. 2007). In addition to the semi annual peak, the meridional mean zonal wind has  
<sup>125</sup> an additional annual peak.<sup>1</sup>

<sup>126</sup> This clearly shows that there exists a broad spectrum of time scales in the forcing. In this paper,  
<sup>127</sup> we argue that the SO response to changing wind lies between the two limits of “Ekman” (fast)  
<sup>128</sup> response and an “eddy saturated” (slow) response, and the mechanisms that govern this response  
<sup>129</sup> are different depending on the frequency of forcing. In the limit of high frequency forcing, the  
<sup>130</sup> ocean responds by converting all the excess wind work into available potential energy by Ekman  
<sup>131</sup> upwelling and tilting isopycnals, and the isopycnals adjust before energy can be transferred effec-  
<sup>132</sup> tively into the eddies. In the low frequency limit (slow limit), most of the additional wind work is  
<sup>133</sup> converted into eddy kinetic energy via baroclinic eddies. At intermediate forcing frequencies, the  
<sup>134</sup> response goes through a regime shift, depending on how effective the eddies are at extracting en-  
<sup>135</sup> ergy from the wind work through baroclinic instability. To investigate the physical parameters that  
<sup>136</sup> determine this transition between fast and slow response we examine the energetic pathways in-  
<sup>137</sup> volved in transferring wind power into eddies via baroclinic instability, the subsequent dissipation,  
<sup>138</sup> and the timescales on which these processes happen.

<sup>139</sup> Our paper is organized as follows: In section 2 we derive a simple conceptual model of time  
<sup>140</sup> dependent eddy activity based on energetics and introduce a “transfer function” approach to obtain  
<sup>141</sup> the solutions to the simple system of equations. In section 3, we describe the suite of numerical  
<sup>142</sup> experiments used, describe the analysis employed and discuss the results. The results from the  
<sup>143</sup> numerical simulations are compared with the conceptual model in section 4. We summarize the  
<sup>144</sup> results and discuss the implications of the present work in section 5.

---

<sup>1</sup>In the NCEP - NCAR Reanalysis, the two peaks are of comparable strength whereas in the ERA - Interim reanalysis data the semi-annual peak is the dominant peak compared to the peak associated with the seasonal cycle. In addition we also see a peak associated with high frequency diurnal cycle.

<sup>145</sup> **2. Conceptual Model: Fast and Slow Limits**

<sup>146</sup> In this section we derive a theoretical framework for understanding the energetic pathways in-  
<sup>147</sup> volved in the ocean's response to a variable forcing. In this framework we look at the rates at  
<sup>148</sup> which energy is transferred from the wind work input into available potential energy (APE) and  
<sup>149</sup> eddy kinetic energy (EKE) and how these rates are dependent on the timescales considered. Con-  
<sup>150</sup> servation of energy dictates that whatever energy is input into the system via wind work has to be  
<sup>151</sup> used up either to raise the available potential energy or to increase eddy mixing and subsequently  
<sup>152</sup> dissipated. Since APE is related to change in isopycnal slopes, we expect the APE to respond  
<sup>153</sup> quickly to changing winds. APE can be used as a good estimate for stratification and thermo-  
<sup>154</sup> cline depth and we expect this to be correlated with zonal transport ( $U_T$ ) (Abernathay and Cessi  
<sup>155</sup> 2014). EKE, which characterizes the mesoscale eddy activity, responds more slowly since eddies  
<sup>156</sup> are formed as a consequence of baroclinic instability.

<sup>157</sup> For our present study, we consider an adiabatic channel flow forced at the surface by oscillating  
<sup>158</sup> winds and ignore all diapycnal fluxes of buoyancy and surface buoyancy fluxes. By doing so, we  
<sup>159</sup> essentially eliminate thermodynamics, and isolating the pure dynamical response of the ocean. Of  
<sup>160</sup> course the real SO will also have time dependent thermodynamics (Ferreira et al. 2014) which  
<sup>161</sup> could be investigated by applying the same approach in future studies.

<sup>162</sup> Following on similar lines from Lorenz (1960); Holland (1978), the energy budget for the system  
<sup>163</sup> is expressed as:

$$\frac{d(APE)}{dt} = \text{Wind work} - C \quad (1)$$

$$\frac{d(EKE)}{dt} = C - D \quad (2)$$

165 where Wind work =  $\frac{1}{\rho_0} \iint_{dA} (\boldsymbol{\tau} \cdot \mathbf{u})$ , D is the rate of frictional dissipation and  $C = \iiint_{dV} (w' b')$   
 166 is the conversion term which denotes the rate at which energy is converted from APE to EKE. A  
 167 derivation of this system of equations is shown in the Appendix. In these simple set of equations,  
 168 we see that the rate of change of APE is directly proportional to the wind power input and energy  
 169 is removed from APE into EKE by means of the conversion term C, which acts as a sink of energy  
 170 in the APE budget and a source in the EKE budget. D is the rate at which energy is dissipated by  
 171 frictional drag.

172 First, we consider the conversion term and try to estimate the parameters from scaling argue-  
 173 ments consistent with previous studies (Gent and Mcwilliams 1990; Gent et al. 1995; Tandon and  
 174 Garrett 1996).

$$\overline{w'b'} = -\overline{v'b'} \frac{\overline{b_y}}{\overline{b_z}} \quad (3)$$

175 Using a Gent McWilliams (Gent and Mcwilliams 1990; Gent 2011) type closure

$$-\overline{v'b'} = K_{GM} \overline{b_y} \quad (4)$$

176 we can rewrite the conversion term as

$$\overline{w'b'} = K_{GM} \frac{\overline{b_y^2}}{\overline{b_z}} \quad (5)$$

177 If APE is defined as

$$APE = \frac{1}{2} \int_0^H \frac{\overline{b'^2}}{\partial \bar{b}/\partial z} dz \quad (6)$$

178 where by definition,  $b = \bar{b} + b'$ . From a first order Taylor series expansion we can also write  
 179  $b = \bar{b} + \frac{\partial \bar{b}}{\partial y} y$ . This implies

$$APE = \frac{1}{2} \int_0^H \frac{\overline{(y \frac{\partial \bar{b}}{\partial y})^2}}{\partial \bar{b}/\partial z} dz$$

<sup>180</sup> Now since  $APE \propto \overline{b_y}^2 / \overline{b_z}$ , we can rewrite the conversion term as

$$\overline{w' b'} \approx \frac{K_{GM} (APE)}{L_y^2} \quad (7)$$

<sup>181</sup> For this kind of eddy closure, we obtain a constant eddy diffusivity ( $K_{GM}$ ) which is independent  
<sup>182</sup> of EKE and therefore neglects eddy feedbacks. So the conversion of APE to EKE is linearly  
<sup>183</sup> proportional to the APE with a constant of proportionality, which we call  $c$  and which has units  
<sup>184</sup> of inverse time. For ease of representation, we denote  $f(t)$  as the external forcing (wind power  
<sup>185</sup> input),  $P(t)$  the APE and  $K(t)$  the EKE. For now, we also assume that EKE is dissipated linearly  
<sup>186</sup> (i.e. linear bottom drag), with a frictional timescale  $r$  (units of inverse time). For this case we can  
<sup>187</sup> express the energy budget as

$$\frac{dP(t)}{dt} = f(t) - cP(t) \quad (8)$$

$$\frac{dK(t)}{dt} = cP(t) - rK(t) \quad (9)$$

<sup>188</sup> Motivated by an analogy to linear time invariant electrical signals (Girod et al. 2001) we derive  
<sup>189</sup> the “transfer functions” for the outputs, namely  $P(t)$  (APE) and  $K(t)$  (EKE) for a periodic input  
<sup>190</sup> signal  $f(t)$ , (wind power) with input frequency  $\omega$ . This is accomplished by simply taking the  
<sup>191</sup> Fourier transform of the Equations 8 and 9. For detailed derivations the reader is referred to the  
<sup>192</sup> Appendix. The solutions for the complex amplitudes of  $P(t)$  and  $K(t)$  (denoted by  $\hat{P}$  and  $\hat{K}$ ) are  
<sup>193</sup> given by  
<sup>194</sup>

$$\hat{P}(\omega) = |\hat{P}(\omega)| e^{\phi_P(\omega)} = \frac{c - i\omega}{c^2 + \omega^2} \hat{f}(\omega) \quad (10)$$

$$\hat{K}(\omega) = |\hat{K}(\omega)| e^{\phi_K(\omega)} = \frac{rc - \omega^2 - i\omega(r+c)}{(rc - \omega^2)^2 + \omega^2(r+c)^2} c \hat{f}(\omega) \quad (11)$$

195 This complex amplitude can be thought of as comprised of a real amplitude and a real phase, both  
 196 of which are functions of  $\omega$ . The gains (normalized amplitudes of APE and EKE with respect  
 197 to wind work,  $|\hat{P}|$  and  $|\hat{K}|$ ) and phase shifts ( $\phi_P$  and  $\phi_K$ ) for  $P(t)$  and  $K(t)$  with respect to  $f(t)$   
 198 are calculated and plotted in figure 2. Here we see that in the absence of eddy feedbacks, in  
 199 the low frequency limit, the EKE reaches a maximum value at some normalized frequency. The  
 200 maximum EKE in the system is determined by the linear drag coefficient. This is expected since  
 201 the maximum value of EKE that can be attained by the system is constrained by the rate at which  
 202 energy is removed from the system by frictional dissipation (Abernathay and Cessi 2014). As  
 203 seen in Figure 2, EKE saturates at the largest value for the smallest drag coefficient and equals the  
 204 maximum APE when  $r = c$ , *i.e.* when frictional dissipation rate is the same as the rate at which  
 205 energy is transferred from APE to EKE.

206 However, this simplified system fails to capture an important nonlinear interaction brought about  
 207 by the eddy feedbacks. Since the conversion term used in this case is simply proportional to APE,  
 208 eddies can't directly affect this term. We can incorporate eddy feedbacks into the transfer term by  
 209 invoking mixing-length arguments which account for the mixing-suppression effect of eddy prop-  
 210 agation (Ferrari and Nikurashin 2010; Klocker et al. 2012; Abernathey et al. 2013; Klocker and  
 211 Abernathey 2014; Abernathey and Ferreira 2015). For such kind of closure we replace the con-  
 212 stant GM eddy diffusivity ( $K_{GM}$ ) by an effective eddy diffusivity ( $K_{eff}$ ) (Abernathay and Ferreira

<sub>213</sub> 2015)

$$K_{eff} = \Gamma_{mix} v_{rms} L_{mix} \quad (12)$$

<sub>214</sub> with  $\Gamma$  is a constant, called mixing efficiency and  $L_{mix}$  is the mixing length which is related to  
<sub>215</sub> eddy length scales.  $v_{rms}$  is related to EKE as  $v_{rms} = |v'|^2^{1/2} = (EKE)^{1/2}$ . (For more efficient  
<sub>216</sub> eddy feedback, we can write a Taylor series expansion and rewrite  $K_{eff} \propto (EKE)$ ). Using this  
<sub>217</sub> relationship, we modify the conversion term as

$$\overline{w'b'} = \frac{K_{eff} (APE)}{L_y^2} \approx k(APE)(EKE)^{1/2} \quad (13)$$

<sub>218</sub> where all the constants  $\Gamma_{mix}$ ,  $L_{mix}$  and  $L_y$  are incorporated into the constant  $k$  as

$$k \approx \Gamma_{mix} \frac{L_{mix}}{L_y^2} \quad (14)$$

<sub>219</sub> For a more general case we can write

$$\overline{w'b'} \approx k(APE)(EKE)^\alpha \quad (15)$$

<sub>220</sub> Here  $\alpha$  ( $0 < \alpha < 1$ ) is used to indicate the efficiency of eddy restratification and a higher  $\alpha$   
<sub>221</sub> indicates higher sensitivity of the transfer to the value of EKE and higher eddy feedback. So to  
<sub>222</sub> study the role of eddy feedbacks in the context of our present problem we modify equations 8 and  
<sub>223</sub> 9 as

$$\frac{dP}{dt} = f - kPK^\alpha \quad (16)$$

$$\frac{dK}{dt} = kPK^\alpha - r_1 K^\beta \quad (17)$$

<sup>225</sup> For a more general description,  $\beta$  is varied depending upon the drag power law used (linear or  
<sup>226</sup> quadratic). It can be shown that for linear drag,  $\beta = 1$  and for quadratic drag,  $\beta = 3/2$

The steady state solution is obtained by taking time mean of equations 16 and 17

$$\bar{f} = k \bar{P} \bar{K}^\alpha,$$

$$r_1 \bar{K}^\beta = k \bar{P} \bar{K}^\alpha$$

Neglecting time varying correlations between EKE and APE, this can be approximated linearly as

$$f = k \bar{P} \bar{K}^\alpha,$$

$$r_1 \bar{K}^\beta = k \bar{P} \bar{K}^\alpha$$

<sup>227</sup> which can be used to solve for the constants  $k$  and  $r_1$

$$k = \frac{\bar{f}}{\bar{K}^\alpha \bar{P}}$$

<sup>228</sup>

$$r_1 = \frac{k \bar{P} \bar{K}^\alpha}{\bar{K}^\beta}$$

<sup>229</sup> Linearizing about a time mean state (denoted by overbar) and an oscillating part (denoted by  
<sup>230</sup> primes) as

$$\begin{aligned} k P K^\alpha &= k (\bar{P} + P') (\bar{K} + K')^\alpha = k (\bar{P} + P') \bar{K}^\alpha (1 + \alpha \frac{K'}{\bar{K}}) \\ &= k \bar{P} \bar{K}^\alpha + k \alpha \bar{K}^{\alpha-1} \bar{P} K' + k P' \bar{K}^\alpha + k \alpha \bar{K}^{\alpha-1} P' K' \end{aligned}$$

<sup>231</sup>

<sup>232</sup> The time varying equation can be written as

$$\frac{dP'}{dt} = f' - kP'\bar{K}^\alpha - k\alpha\bar{P}\bar{K}^{\alpha-1}K' \quad (18)$$

<sup>233</sup>

$$\frac{dK'}{dt} = kP'\bar{K}^\alpha + k\alpha\bar{P}\bar{K}^{\alpha-1}K' - r_1\beta\bar{K}^{\beta-1}K' \quad (19)$$

<sup>234</sup> We define constants  $c_1 = k\bar{K}^\alpha$  and  $c_2 = k\alpha\bar{P}\bar{K}^{\alpha-1}$  and  $r = r_1\beta\bar{K}^{\beta-1}$ , giving

$$\frac{dP'}{dt} = f' - c_1P' - c_2K' \quad (20)$$

<sup>235</sup>

$$\frac{dK'}{dt} = c_1P' + c_2K' - rK' \quad (21)$$

<sup>236</sup> Firstly, we note that this system of equations is very similar to equations 8 and 9 with an extra  
<sup>237</sup> term and upon setting  $c_2 = 0$  we get back our previous solution without eddy feedbacks. The sum  
<sup>238</sup>  $c_1P' + c_2K'$  is denotes the rate at which energy is transferred from APE to EKE. These two terms  
<sup>239</sup> appear as sinks in the APE budget and as sources in the EKE budget. The first part of this transfer  
<sup>240</sup> rate is  $c_1P'$  which is the energy conversion due to eddy diffusivity of the form given by a GM type  
<sup>241</sup> eddy closure. This dictates the transfer of energy into eddies from the APE caused due to tilted  
<sup>242</sup> isopycnal slopes via baroclinic instability (Abernathay and Cessi 2014; Klocker and Abernathay  
<sup>243</sup> 2014) and is related to the baroclinic energy conversion mechanism described in Chelton et al.  
<sup>244</sup> (1998); Smith (2007). This is only dependent on the APE via the isopycnal slope. The second part  
<sup>245</sup>  $c_2K'$  is the eddy feedback rate in our linearized picture and is related to eddy mixing. The constant  
<sup>246</sup>  $c_2$  is dependent both on the steady state (time invariant) APE as well as the steady state EKE.  $r$  is  
<sup>247</sup> the linear frictional drag rate which is also dependent on the steady state EKE in addition to the  
<sup>248</sup> frictional drag coefficient. The Fourier solution is obtained as

$$\left( i\omega + \frac{c_1 c_2}{i\omega - c_2 + r} \right) \hat{P} = \hat{f} \quad (22)$$

$$\left[ c_2 + \frac{(i\omega - c_2 + r)(i\omega + c_1)}{c_1} \right] \hat{K} = \hat{f} \quad (23)$$

249 The gain and phase shift of the APE and EKE for different values of the constants are plotted  
 250 in figure 3. The forcing frequency ( $\omega$ ) is normalized by the transfer rate  $c_1$  in the figure. It is  
 251 observed that for certain choices of  $r$  and  $c_2$ , i.e. when the eddy feedback rate equals the frictional  
 252 dissipation rate( $r = c_2$ ), in addition to the gain in EKE saturating at low frequencies, the gain  
 253 in APE starts dropping below a certain cutoff frequency. This cutoff frequency also decreases  
 254 with decreasing  $r (= c_2)$ . This is quite obvious since with increased rate of eddy feedback (and  
 255 increased dissipation), APE is removed faster (at higher frequencies) into eddies. In general we  
 256 notice that with decreasing  $r$ , in addition to EKE saturating at higher values, the EKE also falls into  
 257 phase with wind slower (i.e. the phase difference approaches 0 at higher frequencies for higher  
 258 rate of frictional dissipation). Another feature observed is the inverse proportionality of the APE  
 259 to forcing frequency ( $\omega$ ) in the high frequency limit. The APE lags the wind in phase by  $\pi/2$  for  
 260 the highest frequencies and the EKE lags by  $\pi$ , barring a few cases. In the low frequency limit  
 261 (over long timescales of forcing), EKE is in phase with the wind.  
 262

263 This conceptual model gives us a framework through which we can understand the energetic  
 264 pathways involved in transferring energy from wind work into eddies by means of tilting isopycnal  
 265 slopes. By exploring the rates of energy transfer in the APE and EKE budget, it helps us to go  
 266 beyond the steady state eddy equilibration and allows to think about the timescales on which these  
 267 processes occur in the transient ocean. Through this parameter space exploration, we try to find  
 268 what determines the timescales over which eddies start becoming important. The relative strengths  
 269 of the constants  $c_1$  and  $c_2$  determine when eddy feedbacks become important and the competition

270 between these two processes sets the timescales of eddy activity in the ocean. To explore this  
271 competition between eddy diffusion and transient eddy mixing in a more realistic sense, we now  
272 turn to numerical simulations of the eddy equilibration process with different time periodic winds.

### 273 3. Numerical Model

274 To examine the applicability of the theoretical framework derived in the previous section, we  
275 use the isopycnal GOLD model of Hallberg and Gnanadesikan (2006) (Hallberg 1997). This  
276 simple isopycnal model can be run at very high resolution (4km horizontal) at a relatively low  
277 computational cost compared to global eddy resolving models. Also, this model allows us to  
278 set diapycnal fluxes to zero, as a result of which we can look at the purely dynamic response  
279 of a stratified ocean to a periodic wind forcing. The choice of isopycnal coordinates makes it  
280 better suited for our analysis compared to QG models used in previous studies by Wilson et al.  
281 (2015) and Hogg et al. (2003, 2008) as it imposes no constraints on isopycnal slope . In addition,  
282 since we assume adiabatic ocean, this kind of reduced gravity model can be considered a decent  
283 approximation for a continuously stratified ocean.

284 The channel setup used for the present work is described in Howard et al. (2015). In these sets  
285 of experiments, the SO is represented as a zonally re-entrant channel with three reduced gravity  
286 layers. The model solves the primitive equations of motion in isopycnal coordinates described in  
287 Killworth and Nanneh (1994) and Ward and Hogg (2011). The reader is referred to Howard et al.  
288 (2015) for details about the numerical setup. We explore a wide range of forcing frequencies using  
289 a zonally invariant oscillating wind stress of the form

$$\tau^x = \left( \tau_0^x + \tau_1^x \sin\left(\frac{2\pi t}{T}\right) \right) \sin\left(\frac{\pi y}{L_y}\right) \quad (24)$$

where  $T$  is the time period of the forcing frequency, and  $L_y$  is the meridional length of our periodic channel. Alternately we can represent the frequency of forced oscillations as  $\omega = \frac{2\pi}{T}$ . A series of ensemble numerical experiments with different forcing frequencies are conducted along with an ensemble of control experiments with a zonally symmetric steady wind. The forcing periods chosen for our experiments are powers of two years. For each forcing period ( $T$ ) experiment,  $M$  ensemble members with different initial conditions are run for  $N_T$  years, so as to have the same number of forcing cycles of integration for each set ( $\frac{N_T \times M}{T}$ ). The oscillating wind experiments consist of six sets with forcing periods  $T \in \{1/4, 1/2, 1, 2, 4, 8\}$  years, along with a set of control runs with steady time invariant wind forcing. The details of the integration time and the number of ensembles used for each of these sets are provided in Table 1. In each of the variable wind forcing experiments the peak wind stress of the half sine jet described in Eqn 24 is chosen to be  $0.2 \text{ Nm}^{-2}$  and the magnitude of the oscillating part of the wind is chosen to be  $0.1 \text{ Nm}^{-2}$ .

The model is run for 10 years forced with a steady wind till spin up and then allowed to run for an additional year before the oscillating wind forcings are imposed. Figure 4 shows the magnitude of the zonally invariant wind stress and the configuration of the bottom topography used in the numerical simulations. A snapshot of the model showing the three isopycnal layers and the relative vorticity in the top layer during spinup is also shown.

From the model variables ( $u$ ,  $v$ ,  $\eta$ ,  $h$ , and  $\tau$ ), the time series for  $EKE$ ,  $PE$ , and wind power is constructed for each ensemble member. This long timeseries contains information about the model behaviour over all timescales present in the problem. The timeseries information is analyzed in two different ways described in the next two sections.

311 *a. Spectral Analysis*

312 A well established and universal method of analyzing long timeseries data is the power spectrum.  
313 By looking at any timeseries data in the spectral space, a comprehensive picture of all timescales  
314 can be obtained. Also, our analytical framework is constructed and solved in the spectral space. So  
315 a more direct comparison is possible if we analyze our numerical simulation results in the spectral  
316 space as well. For these reasons, the obvious first step at analysing the frequency characteristics  
317 of our model ocean's response in EKE, APE to wind power, was to compute the power spectral  
318 density in each of these quantities. The spectrum is computed from each ensemble member using  
319 multi taper spectral methods (Thomson 1982, 2007; nitime 2015). An ensemble mean is then  
320 calculated for the power spectral densities (psd's) over all ensemble members in the spectral space.  
321 The computed power spectrum for all the quantities is shown in figure 5 along with the standard  
322 deviation in averaging over the ensemble members. The error in multitaper spectral estimation of  
323 the long time series have not been shown for ease of representation.<sup>2</sup>

324 The amplitude of oscillation of EKE and PE relative to the amplitude of wind power are  
325 then calculated from the psd at each of the forcing frequencies. Each set of experiments  
326 ( $T \in \{1/4, 1/2, 1, 2, 4, 8\}$  and steady wind forcing) is shown in a different color. As can be ex-  
327 pected from oscillating wind forced experiments, straightaway we see a clear peak in each of  
328 these quantities at the corresponding forcing frequency. The maximum power spectral density in  
329 the wind work input is roughly the same for all the different forcing experiments (which is what we  
330 expect since the wind oscillation amplitude is the same for each experiment). However, the slight  
331 increase in wind power with decreasing forcing frequencies may be attributed to the background  
332 slope of the psd. This background slope is the same for the steady wind forcing experiment and

---

<sup>2</sup>While multitapering reduces estimation bias compared to ensemble averaging by obtaining multiple independent estimates from the same sample, we use ensemble members for computational efficiency. So a compromise is achieved between having a longer timeseries and the number of ensemble members.

333 is therefore attributed to natural variability . As the wind power is computed as the dot product  
334 of the wind stress and the mean zonal velocity, it implies that higher mean zonal velocities for  
335 the lower frequency cases will correlate with the time varying winds, giving a higher wind work.  
336 This is clearly evidenced by higher psd observed in the mean kinetic energy and background zonal  
337 transport in the low frequency experiment cases.

338 A striking feature observed in the power spectrum is the lack of any observable peak in EKE at  
339 higher frequencies ( $T < 1$  year). This shows that at such short timescales of oscillation, EKE does  
340 not respond to wind changes. This is in agreement with our hypothesis. On a side note, we do  
341 observe secondary peaks in some of these quantities at the next highest frequencies.

342 It is useful to mention at this point, that for frequency analysis, PE serves the same purpose as  
343 the APE, since APE is the only oscillating component of the potential energy and the background  
344 potential energy is a constant which only contributes to the steady state mean.

345 The magnitude of the peaks in EKE, APE and mean KE are all different for the different cases.  
346 Since we are interested in the relative power transferred to the EKE and APE, we will examine the  
347 amplitudes in these quantities normalized by the amplitude of wind work. To be more quantita-  
348 tive, in figure 7, we show the maximum amplitude of EKE and APE normalized by the maximum  
349 amplitude of wind energy input at each forcing frequency, plotted as a function of the forcing fre-  
350 quency. This normalized amplitude calculated from the spectra is analogous to the gain described  
351 in our solution of the analytical model. The  $c/\omega$  line ( $c = \text{a constant}$ ) has been included to show  
352 that the simple inverse proportionality of PE with  $\omega$  as predicted by our linear theory does hold in  
353 the limit of high forcing frequency.

354 In the previous section we described the energetic pathways between the wind power, APE and  
355 EKE and showed that while at high frequencies both APE and EKE variability is inversely pro-  
356 portional to forcing frequency, while at lower frequencies the APE starts decreasing (or saturates

357 depending on the choice of parameters) while EKE starts to flatten out. According to our toy  
358 model, at low frequencies (“eddy saturation”) most of the wind energy is transferred to EKE while  
359 little goes into APE. This is indeed what is observed in figure 7.

360 We must note, at this point, that the zonal transport captured by this model is significantly  
361 larger than standard estimates of ACC transport. This is due to the fact that the first baroclinic  
362 Rossby radius of deformation for our imposed stratification is of the order of 56 km, which is  
363 considerably larger than what is observed in the SO. However our aim is not to make quantitative  
364 predictions of the real ACC, but rather to understand timescales of eddy equilibration in response  
365 to periodic wind stress. We therefore look at the barotropic and baroclinic parts of the transport  
366 and obtain the power spectra in these quantities (shown in figure 6). It is seen that while the  
367 psd in barotropic transport exhibits peaks in the corresponding forcing frequency, the peaks in  
368 the baroclinic transport are stronger. In addition, the background slope of the psd of baroclinic  
369 transport resembles the background slope of EKE, while the barotropic transport has an opposite  
370 spectral slope for  $T > 1/4$ .

371 The spectral analysis revealed useful information about the qualitative nature of the amplitude  
372 response in the EKE and APE to variable wind forcing. The power spectra shows that the response  
373 to oscillating winds is dominated by a peak at the oscillation frequency with little or no peak in  
374 EKE at high frequencies and smaller response in APE at lower frequencies. To better understand  
375 the dynamics of this response, and to obtain a more “mechanistic” description of the system, we  
376 now perform a “composite analysis” to examine both the phase and amplitude response of the  
377 forced variability over a forcing period in a simplified setting.

378 b. Composite Analysis

379 For a periodic wind forcing with forcing period  $T$ , the composite in wind work, EKE and PE  
380 is constructed by treating each  $T$  periodic segment in the time series as an independent signal of  
381 length  $T$  and then taking the mean over all such  $T$  periods present in the time series and over all  
382 the  $M$  composite members. Thus for  $M$  ensemble members and  $N_T$  years of integration, this gives  
383 us  $\frac{M \times N_T}{T}$  independent signals of length  $T$  over which we take the mean and standard deviation to  
384 give the composite signal and the error in its estimation. By doing this we effectively reduce the  
385 original signal which is noisy into a smooth periodic signal with period given by the forcing period  
386 (Qiu et al. 2014). This is analogous to isolating a single power component. A schematic is shown  
387 in figure 8 to clearly demonstrate this procedure.

388 Figure 9 (a) to (g) shows the multi ensemble mean of the time series composited over all the  
389 forcing cycles for each set of numerical experiments along with the standard deviation (shown  
390 by the shading) calculated for EKE, PE and wind energy input. The resulting periodic composite  
391 time series is shown for one forcing cycle, for each of the different forcing experiments. An  
392 obvious feature in this figure is that the amplitude of oscillation in EKE and mean KE is very  
393 small (almost absent in the 1/4 year forcing experiment) and appears to increase with decreasing  
394 forcing frequency, in agreement with the results from the power spectral density.

395 The amplitude of oscillation of EKE and PE (and therefore APE, since background PE is non os-  
396 cillating) is computed by calculating the root mean squared (r.m.s.) amplitude and normalized by  
397 the amplitude of the wind energy input. We have shown these normalized amplitudes for each ex-  
398 periment as a function of the forcing frequency for that experiment in figure 11 (a). As with figure  
399 7, the  $c/\omega$  line ( $c = \text{constant}$ ) is plotted along with the figure to show that our theoretical prediction  
400 for inverse proportionality of APE with forcing frequency holds true in the high frequency range.

401 This is in strong agreement with the amplitude characteristics obtained from the spectral analysis  
402 (fig. 7). They differ only at the higher frequencies ( $T < 1$ ) in EKE. This is because the “ampli-  
403 tude” calculated from the peaks in power spectral density is affected by the background slope of  
404 the power spectra. The background slope in the power spectrum is due to natural variability in the  
405 system as is evidenced by the fact that the steady wind forcing case, in which there is no forcing  
406 variability also has the same spectral slope as the other variable wind experiments. We therefore  
407 consider the estimate of amplitude from the composite analysis to be the more robust one.

408 To characterize the phase of the response, the lag correlation of different composite members of  
409 EKE, mean KE, and PE with the wind energy input is then computed to obtain the mean lag in  
410 each of these quantities for each experiment set. This lag (in days) for each experiment, is then  
411 normalized by the corresponding forcing period to calculate the phase shift (in radians) in EKE,  
412 mean KE and PE relative to the wind work (which is in phase with the wind stress by definition).  
413 The standard deviation in this lag correlation over all the composite members is used to represent  
414 the error in this lag. The phase lag along with the computed error is shown in (figure 11(b)).

415 In the limit of high forcing frequencies, it is seen the error in the phase shift calculated from the  
416 lag correlations is higher in comparison to the low frequency cases. This is expected, since, as is  
417 evident from figure 9, the amplitude of oscillation is negligible for high forcing frequencies. As  
418 a result there is significant spread in the lag correlation. It is observed that the while the mean  
419 phase in APE with wind power is zero at low frequency, it is almost exactly out of phase by  $\pi/2$   
420 at the high frequency limit. This is what was predicted by the analytical model. Thus, the phase  
421 response characteristics of the APE (which is a measure of the tilt in isopycnal slopes) calculated  
422 from the numerical simulations is in accordance with our theory. On the other hand, while EKE is  
423 shifted in phase by  $\phi \approx \pi$  at the high frequency limit, the phase difference approaches zero in the  
424 low frequency range.

425 The composites are also calculated for the barotropic and baroclinic parts of the zonal transport  
 426 and shown in figure 10. These composite quantities are represented about a zero mean since  
 427 the mean barotropic and baroclinic transports differ in magnitude. The barotropic part does not  
 428 exhibit significant periodicity and its amplitude of oscillation remains fairly constant with forcing  
 429 frequency. However, the baroclinic part oscillates more at lower forcing frequencies and also falls  
 430 into phase with the wind work. A curious feature observed is that, the envelope of variability in  
 431 barotropic transport exhibits significant periodicity at lower frequencies.

432 In the next section we revisit our simple analytical model and compare with our findings from  
 433 the numerical simulations qualitatively.

#### 434 **4. Comparing Analytical model with Numerical Model**

435 In the analytical model derived in Section 2, the constants  $k$ ,  $c_1$ ,  $c_2$  and  $r$  can be evaluated from  
 436 the steady state balance. Examining equation 20 and 21, we identify 4 possible cases, depending  
 437 on the choices for  $\alpha$  and  $\beta$  which we have described below.

##### 438 **Case 1**

439 For  $\alpha = 1/2$  and  $\beta = 3/2$  (partial eddy saturation and quadratic drag)

$$440 k = \frac{\bar{f}}{\bar{P}K^{1/2}}, r_1 = \frac{k\bar{P}}{\bar{K}}, c_1 = k\bar{K}^{1/2}, c_2 = \frac{k\bar{P}}{2\bar{K}^{1/2}}, \text{ and } r = \frac{3r_1\bar{K}^{1/2}}{2} = \frac{3k\bar{P}}{2\bar{K}^{1/2}}$$

##### 441 **Case 2**

442 For  $\alpha = 1$ , and  $\beta = 3/2$  (total eddy saturation and quadratic drag)

$$443 k = \frac{\bar{f}}{\bar{P}K}, r_1 = \frac{k\bar{P}}{\bar{K}^{1/2}}, c_1 = k\bar{K}, c_2 = k\bar{P}, \text{ and } r = \frac{3r_1\bar{K}^{1/2}}{2} = \frac{3k\bar{P}}{2}$$

##### 444 **Case 3**

445 For  $\alpha = 1/2$ , and  $\beta = 1$  (partial eddy saturation with linear drag)

$$446 k = \frac{\bar{f}}{\bar{P}K^{1/2}}, r_1 = \frac{k\bar{P}}{\bar{K}^{1/2}}, c_1 = k\bar{K}^{1/2}, c_2 = \frac{k\bar{P}}{2\bar{K}^{1/2}}, \text{ and } r = r_1 = k\bar{P}K^{1/2}$$

##### 447 **Case 4**

448 For  $\alpha = 1$ , and  $\beta = 1$  (total eddy saturation with linear drag)

449  $k = \frac{\bar{f}}{\bar{P}K}$ ,  $r_1 = k\bar{P}$ ,  $c_1 = k\bar{K}$ ,  $c_2 = k\bar{P}$ , and  $r = r_1 = k\bar{P}$

450 Using the steady state values calculated from the numerical experiments, for *EKE*, *APE* (sub-  
451 tracting the steady state background *PE* from the long term mean *PE*) and wind work, and plug-  
452 ging those values in equations 22 and 23, we can plot the normalized amplitude and phase for *APE*  
453 and *EKE* for all the cases alongside those obtained from our composite analysis. The constants  
454  $c_1$ ,  $c_2$  and  $r$  all have units of inverse time since they are all denote rates of change of different en-  
455 ergies. For the range of forcing frequencies explored in our experiments inverse  $c_1$  is in the range  
456 550 – 562 days and inverse  $c_2$  ranges from 155 to 158 days for  $\alpha = 1/2$  and 77 to 79 days for  
457  $\alpha = 1$ . Inverse  $r$  on the other hand, is  $\approx 53$  days if quadratic bottom drag law is used and 79 days  
458 for linear drag. As mentioned in section 2,  $c_1$  represents the rate of eddy diffusion via eddy advec-  
459 tion (Gent and Mcwilliams 1990; Gent 2011), while  $c_2$  denotes the rate of eddy mixing through  
460 eddy feedback on the energy cycle. So this shows that while eddy diffusion acts on timescales of  
461 1 – 2 years (slow process), eddy mixing is a much faster ( $\approx 1/4$  yr) process. These two processes  
462 work together towards eddy equilibration in the ocean. Hence, eddy diffusion alone can't capture  
463 the full dynamics of eddy equilibration in the SO and therefore linear baroclinic instability theory  
464 alone can not be used to explain eddy timescales (Chelton et al. 1998; Smith 2007). It is therefore,  
465 the competition between these two processes which sets the timescales of eddy equilibration. But  
466 even so, the fastest process is the frictional dissipation, which accounts for the small amplitude  
467 response in *EKE* at high forcing frequencies. At a high forcing frequency, energy is removed by  
468 bottom friction faster than the time required for eddy mixing. In addition, at forcing frequencies  
469 higher than  $T = 2$  yrs, eddy diffusion is inefficient, which also explains the small amplitudes of  
470 oscillation in *EKE* (figure 9) and the absence of peaks in the power spectra of *EKE* (figure 5) at  
471 higher forcing frequencies.

472 Our numerical model implements a quadratic drag law. So we only focus on cases 1 and 2.  
473 We compare the results from the numerical experiment along with our toy model using the steady  
474 state values derived from our numerical experiment in figure 12. The numerical simulation results  
475 agree quite well with the conceptual model. The only place where we see disagreement between  
476 the numerical model and the analytic model is at the high frequencies in EKE. However, it needs  
477 to be noted that at the high frequency end the envelope of error is quite large, since the EKE  
478 barely oscillates at such high frequency of forcing, as can be seen from figures 5 and 9. In general  
479 the numerical model is seen to transfer energy more efficiently into eddies than that predicted  
480 by the analytic model. The most notable feature is the fact that at low frequencies of oscillation  
481 the amplitude of oscillation of APE actually decreases while the EKE flattens out. However, the  
482 strong agreement in the nature of the response in phase as well as amplitude predicted by the  
483 analytic model and those obtained from numerical simulations, supports our initial hypothesis and  
484 our proposed energetic mechanism.

## 485 5. Discussion and Conclusion

486 We have explored the adiabatic SO response under oscillating wind stresses through idealized  
487 numerical modeling, with the goal of understanding the timescales of mesoscale eddy equilibra-  
488 tion. We have proposed a hypothesis for the transient ocean response being between the two limits  
489 of Ekman and eddy saturated response. We developed a conceptual model of the energetic path-  
490 ways between wind power, EKE and APE in the interior ocean and devised a “transfer function”  
491 for the mesoscale eddies. This hypothesis and conceptual energetic framework was tested using  
492 a suite of ensemble numerical simulations of a channel ocean subjected to oscillating winds with  
493 different forcing frequencies. We used composite time series analysis to characterize the phase and  
494 amplitude response of APE, EKE and wind work. We find that in the high frequency limit, there

495 is energy exchange with APE and the subsequent conversion to EKE is small. This shows that  
496 in the limit of high forcing frequency the mesoscale eddies do not get enough time to efficiently  
497 remove energy from the wind energy input. In the other limit, the eddies are efficient at removing  
498 energy from the wind stress and, as is evidenced by the dip in APE at the 8 year forcing in figure  
499 12, more energy is transferred to EKE in comparison to APE as the forcing gets slower. The phase  
500 characteristics indicate that in the low frequency limit, although the energy conversion to EKE is  
501 more efficient, the APE still leads EKE in phase. In the high frequency limit APE extracts energy  
502 from the wind at a phase lag of  $\pi/2$ , by means of tilting isopycnals, while the eddies are fairly  
503 inefficient at extracting energy from the wind on such short timescales and are almost exactly out  
504 of phase with the wind stress at such high frequencies.

505 By constructing a linearized framework for the energetic pathway between wind power APE,  
506 EKE and the subsequent dissipation, a mechanistic picture of the energy transfer process is ob-  
507 tained which is expressed in terms of three constants  $c_1$ ,  $c_2$  and  $r$  which denote the three key  
508 processes involved. These three processes acting in conjunction determine the timescale of eddy  
509 equilibration process.  $c_1$  is the rate of eddy dissipation (slow),  $c_2$  of eddy mixing (fast) and  $r$  is  
510 the rate of dissipation by frictional drag (fastest). At high frequencies of forcing, eddy diffusion  
511 is ineffective and frictional dissipation removes wind energy before eddies can effectively convert  
512 wind power to EKE. At forcing periods higher than two years eddy diffusion becomes important.  
513 The formation of eddies and eddy advection then leads to eddy feedback via eddy mixing, which,  
514 in conjunction with eddy diffusion acts to convert energy more effectively into EKE due to more  
515 vigorous eddy activity. As a result, when the forcing period is increased beyond four years a com-  
516 plete shift in regime is observed, where more energy is converted into EKE and the amplitude of  
517 oscillation of APE decreases. When the forcing period is eight years, it effectively means that the

518 wind power is increasing for half of that period ( $\approx 4$  years). This gives the eddies enough time to  
519 effectively convert wind power to EKE from the tilted isopycnal slopes.

520 Furthermore, if we look at the composite of zonal transport in figure 10, and their power spectral  
521 density in figure 6, over higher frequencies the amplitude of oscillations in the barotropic and baro-  
522 clinic transport are comparable, while in the low frequency limit, the oscillations in transport are  
523 primarily due to the baroclinic part. In addition, the baroclinic transport also falls into phase with  
524 wind power at low frequencies indicating that the mesoscale eddy activity is primarily driven by  
525 baroclinic instability. Upon closer inspection of figure 10, we see that the variability in barotropic  
526 transport also exhibits strong periodicity at lower forcing frequencies, which might be explained  
527 by the fact that the eddy activity associated with the increased baroclinic instability, might drive  
528 a secondary barotropic instability, which causes the variability in transport to diverge in response  
529 to increasing winds. Further study need to be done to look at this eddy bolus flux and its role in  
530 determining the strength of the ACC transport. This also goes on to show that linear baroclinic  
531 instability theory alone can't be used explain the eddy length and timescales (Smith 2007).

532 By conducting ensemble numerical experiments of an idealized adiabatic channel ocean to a va-  
533 riety of oscillating wind forcings we have devised a “transfer function” approach for the mesoscale  
534 eddies. The results from our numerical simulations support our “two limits” hypothesis and show  
535 that the transient ocean response goes from an Ekman response state to an “eddy saturated” state  
536 through a smooth regime shift predicted by a response function. The response function calculated  
537 from the long term mean APE, EKE, and wind power using a simple theory shows considerable  
538 agreement with our findings from numerical simulations. Results from numerical experiments  
539 show that the oscillation in APE has a maximum amplitude around a forcing period of 4 years and  
540 starts dropping at lower forcing frequencies while the EKE exhibits “saturation” at the low fre-  
541 quencies. This transfer function, thus derived, can be used to calculate eddy response amplitude

542 and phase, when the system is forced with a superposition of different forcing frequencies with-  
543 out the need to actually run the model. The key ingredients for formulating this transfer function  
544 are the constants  $c_1$ ,  $c_2$  and  $r$ . In our paper we evaluated these constants from the time averaged  
545 values of *EKE*, *PE* and wind work in the context of a reduced gravity model. These constants can  
546 be evaluated similarly from long time numerical simulations with more realistic models or from  
547 observational estimates for the real ocean and a similar transfer function can be devised for the  
548 real ocean.

549 In a recent study by Eden and Greatbatch (2008), a parameterisation for the effect of mesoscale  
550 eddies is derived for the interior ocean, that goes beyond a constant prescribed value of  $K$  (Gent  
551 and Mcwilliams 1990). This is based on a mixing length approach, and takes into account, the  
552 turbulent energy budget. The closure is given by a prognostic equation for *EKE*, from which,  
553 together with a diagnostic equation for the eddy length scale, a diffusivity,  $K$  (related to isopycnal  
554 thickness diffusivity of the GM parameterisation (Gent and Mcwilliams 1990; Gent 2011)) is  
555 calculated using the mixing length assumption. The *EKE* equation is integrated prognostically in  
556 a non-eddy-resolving model, simply as an additional tracer.

557 While it has been shown that maximum eddy activity and baroclinic instability are non local in  
558 space (Abernathy and Cessi 2014), previous satellite altimetry and modelling studies (Meredith  
559 and Hogg 2006; Hogg et al. 2008) as well as our results show that they are also not collocated  
560 in time either, indicating that eddy generation and dissipation are separated in phase. Existing  
561 parameterizations which include time dependent mesoscale eddy closure schemes for eddy pa-  
562 rameterization (Berloff 2015) are unable to account for this “memory effect” of eddies. In this  
563 paper we provide a mechanistic explanation for this non local temporal behavior in eddy activity.  
564 Our analytical framework can be used to include this “eddy memory” effect in existing parameter-

565 ization schemes, and help in obtaining a more complete theory for mesoscale eddy equilibration  
566 and baroclinic instability.

567 Another key ingredient of the eddy equilibration problem in the SO, which we have ignored  
568 in this study, is thermodynamics. The real ocean is not purely dynamic in its response. It is  
569 widely accepted that the variability of sea surface temperature (SST) is important in determining  
570 the present state of the climate from past records and predicting future climate change. While  
571 there is agreement between multi-proxy estimates of SST variability and general circulation model  
572 estimates on synoptic and annual timescales, they have been shown to diverge strongly on longer  
573 timescales (Laepple and Huybers 2014). In addition to there being multiple timescales in the  
574 SO dynamic response, there also exists multiple timescales in the SO thermodynamic response  
575 to changing winds (Ferreira et al. 2014), which has been investigated through coupled climate  
576 models. The complicated nature of the multiple timescales in both mechanical and thermodynamic  
577 forcings and the multiple feedbacks associated with diabatic response, coupled with the response  
578 to changes in sea ice and ozone hole depletion (Polvani and Smith 2013; Solomon et al. 2015)  
579 makes the SO a challenging area of research which merits future endeavors. In this study we  
580 show how only a purely dynamic response to a purely mechanical forcing can exhibit different  
581 behavior depending on timescales. The mechanism of the dynamic response characteristics via  
582 energy transfer functions described in our present work can be used in conjunction with existing  
583 modelling studies exploring the roles of thermodynamic forcings associated with sea ice changes  
584 and ozone depletion, to formulate a general and more complete theory for SO response and its role  
585 on overturning circulation.

586 *Acknowledgments.* This study has been funded by a Frontiers in Earth System Dynamics (FESD)  
587 grant from the US National Science Foundation. The computations were carried out partially

588 with high-performance computing support provided by NCAR's Computational and Information Systems Laboratory (CISL), and partially with Columbia University Information Technology  
 589 (CUIT)'s High Performance Computing (HPC) Cluster service.  
 590

## 591 APPENDIX A

### 592 **Derivation of Analytical Formulation from Kinematics**

593 In section 2 we described a simple analytical model involving energetic pathways. Here we  
 594 derive the energy equations described by equations 1 and 2.

595 The equations of motion are written as

$$596 \frac{D\mathbf{u}}{Dt} + \mathbf{f} \times \mathbf{u} = -\nabla\phi + \frac{1}{\rho_0}\nabla\tau \quad (A1)$$

$$597 \frac{Db}{Dt} = 0 \quad (A2)$$

$$598 \frac{\partial\phi}{\partial z} = b \quad (A3)$$

$$599 \frac{\partial w}{\partial z} = -\frac{\partial u}{\partial x} - \frac{\partial v}{\partial y} \quad (A4)$$

600 Linearizing as  $u = \bar{u} + u'$ ,  $w = w_{Ek} + w'$  and  $b = \bar{b}(z) + b'(x, y, z, t)$ , the thermodynamic equation becomes

$$601 \frac{Db'}{Dt} = -N^2 w = -\frac{\partial \bar{b}}{\partial z} w = -\frac{\partial \bar{b}}{\partial z} (w_{Ek} + w') \quad (A5)$$

602 The perturbation momentum equation is written as

$$603 \frac{D\mathbf{u}'}{Dt} + \mathbf{f} \times \mathbf{u}' = -\nabla\phi' + \frac{1}{\rho_0}\nabla\tau' \quad (A6)$$

602 Multiplying equation A5 by  $\frac{b'}{\frac{\partial b}{\partial z}}$  and integrating over the volume we obtain the APE equation  
 603 written as

$$\frac{D(APE)}{Dt} = \frac{1}{2} \frac{D}{Dt} \iiint_{dV} \left( \frac{b'^2}{\frac{\partial b}{\partial z}} \right) = - \iiint_{dV} w_{Ek} b' - \iiint_{dV} w' b' \quad (\text{A7})$$

604 The EKE equation is obtained by taking the dot product of equation A6 with  $\mathbf{u}'$

$$\frac{D(EKE)}{Dt} = \frac{1}{2} \frac{D}{Dt} (u'^2 + v'^2) = \frac{1}{\rho_0} \iint_{dA} \tau_x u_s - \frac{1}{\rho_0} \iint_{dA} \tau_b u_b + \iiint_{dV} w \frac{\partial \phi'}{\partial z} \quad (\text{A8})$$

605 where  $\tau_x$  is the zonal wind stress,  $u_s$  is the zonal velocity of the surface layer of the ocean,  $\tau_b$  is the  
 606 bottom frictional drag, and  $u_b$  is the bottom velocity. To derive this we have used the continuity  
 607 equation and the fact  $\partial(u\phi)/\partial x$ ,  $\partial(v\phi)/\partial y$  and  $\partial(w\phi)/\partial z$  all vanish upon integrating over the  
 608 volume. Using the relation  $\frac{\partial \phi'}{\partial z} = b'$  and writing  $w = w_{Ek} + w'$ , we can rewrite this as

$$\frac{D(EKE)}{Dt} = \frac{1}{\rho_0} \iint_{dA} \tau_x u_s - \frac{1}{\rho_0} \iint_{dA} \tau_b u_b + \iiint_{dV} w_{Ek} b' + \iiint_{dV} w' b' \quad (\text{A9})$$

Next we note that the Ekman upwelling vertical velocity can be expressed as

$$w_{Ek} = -\frac{1}{\rho_0 f} \frac{\partial \tau_x}{\partial y}$$

609 This relation is used to show that

$$\iiint_{dV} w_{Ek} b' = -\frac{1}{\rho_0} \iint_{dA} \tau_x u_s \quad (\text{A10})$$

<sup>610</sup> Using this relation the APE budget is written as

$$\frac{D(APE)}{Dt} = \frac{1}{\rho_0} \iint_{dA} \tau_x u_s - \iiint_{dV} w' b' \quad (\text{A11})$$

<sup>611</sup> and the EKE equation as

$$\frac{D(EKE)}{Dt} = \iiint_{dV} w' b' - \frac{1}{\rho_0} \iint_{dA} \tau_b u_b \quad (\text{A12})$$

<sup>612</sup> In the context of our three layer adiabatic ocean, Potential Energy is evaluated as :

$$PE = \frac{1}{2} \left\langle \left\langle \frac{\sum_{k=1}^3 g_k \eta_k^2}{\sum_{k=1}^3 h_k} \right\rangle \right\rangle \quad (\text{A13})$$

<sup>613</sup> The Eddy Kinetic Energy is defined as:

$$EKE = \frac{1}{2} \left\langle \left\langle \frac{\sum_{k=1}^3 h_k (u'_k)^2 + (v'_k)^2}{\sum_{k=1}^3 h_k} \right\rangle \right\rangle \quad (\text{A14})$$

<sup>614</sup> where

$$\langle\langle \bullet \rangle\rangle = \frac{1}{L_x L_y} \int_0^{L_y} dy \int_0^{L_x} dx (\bullet)$$

<sup>615</sup> The subscripts denote the layers,  $\eta$  is the interface height relative to mean sea level,  $h$  is the layer

<sup>616</sup> thickness, and  $g_k$  the reduced gravity of layer  $k$ .

<sup>617</sup>

## APPENDIX B

<sup>618</sup>

### Solution using transfer function

619 Here we briefly describe the solution of the APE and EKE equation using the transfer function  
 620 approach. We illustrate the solution procedure with the simple energy budget (without eddy feed-  
 621 back) with the conversion rate being linearly proportional to APE

$$\frac{dP}{dt} = f(t) - cP \quad (\text{B1})$$

$$\frac{dK}{dt} = cP - rK \quad (\text{B2})$$

622 We take the Fourier transform, thereby assuming periodic solutions. (The initial value problem  
 623 can instead be solved with a Laplace transform.)

$$f = \hat{f} e^{i\omega t}$$

$$P = \hat{P} e^{i\omega t}$$

$$K = \hat{K} e^{i\omega t}$$

627 The energy equations become

$$i\omega \hat{P} = \hat{f} - c\hat{P} \quad (\text{B3})$$

$$i\omega \hat{K} = c\hat{P} - r\hat{K} \quad (\text{B4})$$

629 The solution is

$$\hat{P} = \frac{c - i\omega}{c^2 + \omega^2} \hat{f} \quad (\text{B5})$$

$$\hat{K} = \frac{rc - \omega^2 - i\omega(r+c)}{(rc - \omega^2)^2 + \omega^2(r+c)^2} c\hat{f} \quad (\text{B6})$$

$$\hat{K} = \frac{\hat{f}c_1}{-\omega^2 + rc_1 + i\omega(c_1 - c_2 + r)} \quad (\text{B7})$$

631

$$\hat{P} = \frac{\hat{f}(i\omega - c_2 + r)}{-\omega^2 + rc_1 + i\omega(c_1 - c_2 + r)} \quad (\text{B8})$$

632 **References**

- 633 Abernathey, R., and P. Cessi, 2014: Topographic Enhancement of Eddy Efficiency in Baroclinic  
 634 Equilibration. *Journal of Physical Oceanography*, **44**, 2107 – 2126.
- 635 Abernathey, R., and D. Ferreira, 2015: Southern ocean isopycnal mixing and ventilation  
 636 changes driven by winds. *Geophysical Research Letters*, **42** (23), 10,357–10,365, doi:10.1002/  
 637 2015GL066238, URL <http://dx.doi.org/10.1002/2015GL066238>, 2015GL066238.
- 638 Abernathey, R., D. Ferreira, and A. Klocker, 2013: Diagnostics of isopycnal mixing in a circumpolar  
 639 channel. *Ocean Modelling*, **72**, 1 – 16, doi:<http://dx.doi.org/10.1016/j.ocemod.2013.07.004>,  
 640 URL <http://www.sciencedirect.com/science/article/pii/S1463500313001200>.
- 641 Abernathey, R., J. Marshall, and D. Ferreira, 2011: The dependence of Southern Ocean meridional  
 642 overturning on wind stress. *Journal of Physical Oceanography*, **41** (12), 2261–2278.
- 643 Berloff, P., 2015: Dynamically consistent parameterization of mesoscale eddies. part i: Simple  
 644 model. *Ocean Modelling*, **87**, 1 – 19, doi:<http://dx.doi.org/10.1016/j.ocemod.2014.12.008>, URL  
 645 <http://www.sciencedirect.com/science/article/pii/S1463500314001954>.
- 646 Boning, C. W., A. Dispert, M. Visbeck, S. R. Rintoul, and F. U. Schwarzkopf, 2008: The response  
 647 of the antarctic circumpolar current to recent climate change. *Nature Geosci*, **1** (12), 864–869,  
 648 URL <http://dx.doi.org/10.1038/ngeo362>.

- 649 Chelton, D. B., R. A. deSzoeke, M. G. Schlax, K. El Naggar, and N. Siwertz, 1998: Geographical variability of the first baroclinic rossby radius of deformation. *Journal of Physical Oceanography*, **28** (3), 433–460, doi:10.1175/1520-0485(1998)028<0433:GVOTFB>2.0.CO;2,  
650 URL [http://dx.doi.org/10.1175/1520-0485\(1998\)028<0433:GVOTFB>2.0.CO;2](http://dx.doi.org/10.1175/1520-0485(1998)028<0433:GVOTFB>2.0.CO;2).
- 651  
652  
653 Chidichimo, M. P., K. A. Donohue, D. R. Watts, and K. L. Tracey, 2014: Baroclinic transport  
654 time series of the antarctic circumpolar current measured in drake passage. *Journal of Physical  
655 Oceanography*, **44** (7), 1829–1853, doi:10.1175/JPO-D-13-071.1, URL <http://dx.doi.org/10.1175/JPO-D-13-071.1>.
- 656  
657 Cunningham, S. A., S. G. Alderson, B. A. King, and M. A. Brandon, 2003: Transport and  
658 variability of the antarctic circumpolar current in drake passage. *Journal of Geophysical Research: Oceans*, **108** (C5), n/a–n/a, doi:10.1029/2001JC001147, URL <http://dx.doi.org/10.1029/2001JC001147>, 8084.
- 659  
660  
661 Eden, C., and R. J. Greatbatch, 2008: Towards a mesoscale eddy closure. *Ocean Modelling*, **20** (3),  
662 223 – 239, doi:<http://dx.doi.org/10.1016/j.ocemod.2007.09.002>, URL <http://www.sciencedirect.com/science/article/pii/S1463500307001163>.
- 663  
664 Farneti, R., and T. L. Delworth, 2010: The role of mesoscale eddies in the remote oceanic response  
665 to altered southern hemisphere winds. *Journal of Physical Oceanography*, **40** (10), 2348–2354,  
666 doi:10.1175/2010JPO4480.1, URL <http://dx.doi.org/10.1175/2010JPO4480.1>.
- 667  
668 Ferrari, R., and M. Nikurashin, 2010: Suppression of eddy diffusivity across jets in the southern  
669 ocean. *Journal of Physical Oceanography*, **40** (7), 1501–1519, doi:10.1175/2010JPO4278.1,  
URL <http://dx.doi.org/10.1175/2010JPO4278.1>.

- 670 Ferreira, D., J. Marshall, C. M. Bitz, S. Solomon, and A. Plumb, 2014: Antarctic ocean and sea ice  
671 response to ozone depletion: A two-time-scale problem. *Journal of Climate*, **28** (3), 1206–1226.
- 672 Gent, P. R., 2011: The gentmcwilliams parameterization: 20/20 hindsight. *Ocean Mod-  
673 elling*, **39** (12), 2 – 9, doi:<http://dx.doi.org/10.1016/j.ocemod.2010.08.002>, URL <http://www.sciencedirect.com/science/article/pii/S1463500310001253>, modelling and Understanding the  
674 Ocean Mesoscale and Submesoscale.
- 675
- 676 Gent, P. R., and J. C. Mcwilliams, 1990: Isopycnal mixing in ocean circulation models. *Journal of  
677 Physical Oceanography*, **20** (1), 150–155, doi:[10.1175/1520-0485\(1990\)020<0150:IMIOCM>2.0.CO;2](https://doi.org/10.1175/1520-0485(1990)020<0150:IMIOCM>2.0.CO;2). URL [http://dx.doi.org/10.1175/1520-0485\(1990\)020<0150:IMIOCM>2.0.CO;2](http://dx.doi.org/10.1175/1520-0485(1990)020<0150:IMIOCM>2.0.CO;2).
- 678
- 679 Gent, P. R., J. Willebrand, T. J. McDougall, and J. C. McWilliams, 1995: Parameterizing  
680 eddy-induced tracer transports in ocean circulation models. *Journal of Physical Oceanogra-  
681 phy*, **25** (4), 463–474, doi:[10.1175/1520-0485\(1995\)025<0463:PEITTI>2.0.CO;2](https://doi.org/10.1175/1520-0485(1995)025<0463:PEITTI>2.0.CO;2), URL [http://dx.doi.org/10.1175/1520-0485\(1995\)025<0463:PEITTI>2.0.CO;2](http://dx.doi.org/10.1175/1520-0485(1995)025<0463:PEITTI>2.0.CO;2).
- 682
- 683 Girod, B., R. Rabenstein, and A. Stenger, 2001: *Signals and Systems*. 2nd ed., Chichester: Wiley.
- 684 Hallberg, R., 1997: Stable split time stepping schemes for large-scale ocean modeling. *Journal of  
685 Computational Physics*, **135** (1), 54–65.
- 686
- 687 Hallberg, R., and A. Gnanadesikan, 2001: An exploration of the role of transient eddies in  
688 determining the transport of a zonally reentrant current. *Journal of Physical Oceanogra-  
689 phy*, **31** (11), 3312–3330, doi:[10.1175/1520-0485\(2001\)031<3312:AEOTRO>2.0.CO;2](https://doi.org/10.1175/1520-0485(2001)031<3312:AEOTRO>2.0.CO;2), URL [http://dx.doi.org/10.1175/1520-0485\(2001\)031<3312:AEOTRO>2.0.CO;2](http://dx.doi.org/10.1175/1520-0485(2001)031<3312:AEOTRO>2.0.CO;2).
- 690
- 691 Hallberg, R., and A. Gnanadesikan, 2006: The role of eddies in determining the structure and  
response of the wind-driven Southern Hemisphere overturning: Results from the Modeling

- 692 Eddies in the Southern Ocean (MESO) project. *Journal of Physical Oceanography*, **36** (12),  
693 2232–2252.
- 694 Henning, C. C., and G. K. Vallis, 2005: The effects of mesoscale eddies on the stratification and  
695 transport of an ocean with a circumpolar channel. *Journal of Physical Oceanography*, **35** (5),  
696 880–896, doi:10.1175/JPO2727.1, URL <http://dx.doi.org/10.1175/JPO2727.1>.
- 697 Hogg, A. M., M. P. Meredith, D. P. Chambers, E. P. Abrahamsen, C. W. Hughes, and A. K.  
698 Morrison, 2015: Recent trends in the southern ocean eddy field. *Journal of Geophysical Re-*  
699 *search: Oceans*, **120** (1), 257–267, doi:10.1002/2014JC010470, URL <http://dx.doi.org/10.1002/2014JC010470>.
- 700 Hogg, A. M. C., W. K. Dewar, P. D. Killworth, and J. R. Blundell, 2003: A quasi-geostrophic  
701 coupled model (q-gcm). *Monthly weather review*, **131** (10), 2261 – 2278.
- 702 Hogg, A. M. C., M. P. Meredith, J. R. Blundell, and C. Wilson, 2008: Eddy heat flux in the  
703 Southern Ocean: Response to variable wind forcing. *Journal of Climate*, **21** (4), 608–620.
- 704 Holland, W. R., 1978: The role of mesoscale eddies in the general circulation of the ocean—  
705 numerical experiments using a wind-driven quasi-geostrophic model. *Journal of Physical  
706 Oceanography*, **8** (3), 363–392, doi:10.1175/1520-0485(1978)008<363:TROMEI>2.0.CO;2,  
707 URL [http://dx.doi.org/10.1175/1520-0485\(1978\)008<363:TROMEI>2.0.CO;2](http://dx.doi.org/10.1175/1520-0485(1978)008<363:TROMEI>2.0.CO;2).
- 708 Howard, E., A. M. Hogg, S. Waterman, and D. P. Marshall, 2015: The injection of zonal momen-  
709 tum by buoyancy forcing in a Southern Ocean model. *Journal of Physical Oceanography*, **45**,  
710 259–271.
- 711 Johnson, G. C., and H. L. Bryden, 1989: On the size of the Antarctic Circumpolar Current. *Deep  
712 Sea Research Part A. Oceanographic Research Papers*, **36** (1), 39–53.

- 714 Killworth, P. D., and M. M. Nanneh, 1994: Isopycnal momentum budget of the Antarctic Cir-  
715 cumpolar Current in the Fine Resolution Antarctic Model. *Journal of physical oceanography*,  
716 **24** (6), 1201–1223.
- 717 Klocker, A., and R. Abernathey, 2014: Global patterns of mesoscale eddy properties and diffusiv-  
718 ities. *Journal of Physical Oceanography*, **44** (3), 1030–1046, doi:10.1175/JPO-D-13-0159.1,  
719 URL <http://dx.doi.org/10.1175/JPO-D-13-0159.1>.
- 720 Klocker, A., R. Ferrari, and J. H. LaCasce, 2012: Estimating suppression of eddy mixing by mean  
721 flows. *Journal of Physical Oceanography*, **42** (9), 1566–1576, doi:10.1175/JPO-D-11-0205.1,  
722 URL <http://dx.doi.org/10.1175/JPO-D-11-0205.1>.
- 723 Laepple, T., and P. Huybers, 2014: Ocean surface temperature variability: Large model–data  
724 differences at decadal and longer periods. *Proceedings of the National Academy of Sciences*,  
725 **111** (47), 16 682–16 687.
- 726 Langlais, C. E., S. R. Rintoul, and J. D. Zika, 2015: Sensitivity of antarctic circumpolar cur-  
727 rent transport and eddy activity to wind patterns in the southern ocean. *Journal of Physical  
728 Oceanography*, **45** (4), 1051–1067, doi:10.1175/JPO-D-14-0053.1, URL <http://dx.doi.org/10.1175/JPO-D-14-0053.1>.
- 730 Lorenz, E. N., 1960: Energy and numerical weather prediction. *Tellus*, **12** (4), 364–373, doi:10.  
731 1111/j.2153-3490.1960.tb01323.x, URL <http://dx.doi.org/10.1111/j.2153-3490.1960.tb01323.x>.
- 732 X.
- 733 Marshall, D. P., D. R. Munday, L. C. Allison, R. J. Hay, and H. L. Johnson, 2016: Gills model  
734 of the antarctic circumpolar current, revisited: The role of latitudinal variations in wind stress.

735      *Ocean Modelling*, **97**, 37 – 51, doi:<http://dx.doi.org/10.1016/j.ocemod.2015.11.010>, URL <http://www.sciencedirect.com/science/article/pii/S1463500315002346>.

737      Marshall, J., and T. Radko, 2003: Residual-mean solutions for the Antarctic Circumpolar Current  
738      and its associated overturning circulation. *Journal of Physical Oceanography*, **33** (11), 2341–  
739      2354.

740      Meredith, M. P., and A. M. Hogg, 2006: Circumpolar response of Southern Ocean eddy activity  
741      to a change in the Southern Annular Mode. *Geophysical Research Letters*, **33** (16).

742      Meredith, M. P., A. C. Naveira Garabato, A. M. Hogg, and R. Farneti, 2012: Sensitivity of the over-  
743      turning circulation in the southern ocean to decadal changes in wind forcing. *Journal of Climate*,  
744      **25** (1), 99–110, doi:[10.1175/2011JCLI4204.1](https://doi.org/10.1175/2011JCLI4204.1), URL <http://dx.doi.org/10.1175/2011JCLI4204.1>.  
745      1.

746      Morrison, A. K., and A. M. Hogg, 2013: On the relationship between southern ocean over-  
747      turning and acc transport. *Journal of Physical Oceanography*, **43** (1), 140–148, doi:[10.1175/JPO-D-12-057.1](https://doi.org/10.1175/JPO-D-12-057.1), URL <http://dx.doi.org/10.1175/JPO-D-12-057.1>.

749      Munday, D., and X. Zhai, 2015: Sensitivity of southern ocean circulation to wind stress  
750      changes: Role of relative wind stress. *Ocean Modelling*, **95**, 15 – 24, doi:<http://dx.doi.org/10.1016/j.ocemod.2015.08.004>, URL <http://www.sciencedirect.com/science/article/pii/S1463500315001572>.

753      Munday, D. R., H. L. Johnson, and D. P. Marshall, 2013: Eddy saturation of equilibrated circumpo-  
754      lar currents. *Journal of Physical Oceanography*, **43** (3), 507–532, doi:[10.1175/JPO-D-12-095.1](https://doi.org/10.1175/JPO-D-12-095.1),  
755      URL <http://dx.doi.org/10.1175/JPO-D-12-095.1>.

- 756 nitime, 2015: Neuroimaging in python; nitime 0.5.dev documentation. URL \url{[http://nipy.org/nitime/examples/multi\\_taper\\_spectral\\_estimation.html#id1](http://nipy.org/nitime/examples/multi_taper_spectral_estimation.html#id1)}, [Online; accessed 3-January-  
757  
758 2016].
- 759 Pennel, R., and I. Kamenkovich, 2014: On the factors controlling the eddy-induced transport in  
760 the antarctic circumpolar current. *Journal of Physical Oceanography*, **44** (8), 2127–2138, doi:  
761 10.1175/JPO-D-13-0256.1, URL <http://dx.doi.org/10.1175/JPO-D-13-0256.1>.
- 762 Polvani, L. M., and K. L. Smith, 2013: Can natural variability explain observed Antarctic sea ice  
763 trends? New modeling evidence from CMIP5. *Geophysical Research Letters*, **40** (12), 3195–  
764 3199.
- 765 Qiu, B., S. Chen, P. Klein, H. Sasaki, and Y. Sasai, 2014: Seasonal mesoscale and subme-  
766 soscale eddy variability along the north pacific subtropical countercurrent. *Journal of Physical  
767 Oceanography*, **44** (12), 3079–3098, doi:10.1175/JPO-D-14-0071.1, URL <http://dx.doi.org/10.1175/JPO-D-14-0071.1>.
- 768
- 769 Rintoul, S., and A. Naveira-Garabato, 2013: Dynamics of the southern ocean circulation. *Ocean  
770 Circulation and Climate: A 21st Century Perspective. 2nd Ed*, G. Siedler, S. Griffies, J. Gould,  
771 and J. Church, Eds., 103, Academic Press, 471–492, URL <http://eprints.soton.ac.uk/358928/>.
- 772 Smith, K. S., 2007: The geography of linear baroclinic instability in earth’s oceans. *Journal of  
773 Marine Research*, **65**, 655–683.
- 774 Solomon, A., L. M. Polvani, K. L. Smith, and R. P. Abernathey, 2015: The impact of ozone  
775 depleting substances on the circulation, temperature, and salinity of the southern ocean: An  
776 attribution study with cesm1(waccm). *Geophysical Research Letters*, **42** (13), 5547–5555.

- 777 Swart, N. C., and J. C. Fyfe, 2012: Observed and simulated changes in the southern hemi-  
778 sphere surface westerly wind-stress. *Geophysical Research Letters*, **39** (16), n/a–n/a, doi:  
779 10.1029/2012GL052810, URL <http://dx.doi.org/10.1029/2012GL052810>, l116711.
- 780 Tandon, A., and C. Garrett, 1996: On a recent parameterization of mesoscale eddies. *Journal of*  
781 *Physical Oceanography*, **26** (3), 406–411, doi:10.1175/1520-0485(1996)026<406:OARPOM>  
782 2.0.CO;2, URL [http://dx.doi.org/10.1175/1520-0485\(1996\)026<406:OARPOM>2.0.CO;2](http://dx.doi.org/10.1175/1520-0485(1996)026<406:OARPOM>2.0.CO;2).
- 783 Taschetto, A., I. Wainer, and M. Raphael, 2007: Interannual variability associated with semiannual  
784 oscillation in southern high latitudes. *Journal of Geophysical Research: Atmospheres*, **112** (D2),  
785 n/a–n/a, doi:10.1029/2006JD007648, URL <http://dx.doi.org/10.1029/2006JD007648>, d02106.
- 786 Thomson, D., 1982: Spectrum estimation and harmonic analysis. *Proceedings of the IEEE*, **70** (9),  
787 1055–1096, doi:10.1109/PROC.1982.12433.
- 788 Thomson, D., 2007: Jackknifing multitaper spectrum estimates. *Signal Processing Magazine,*  
789 *IEEE*, **24** (4), 20–30, doi:10.1109/MSP.2007.4286561.
- 790 Treguier, A. M., J. Le Sommer, J. M. Molines, and B. de Cuevas, 2010: Response of the southern  
791 ocean to the southern annular mode: Interannual variability and multidecadal trend. *Journal of*  
792 *Physical Oceanography*, **40** (7), 1659–1668.
- 793 Viebahn, J., and C. Eden, 2010: Towards the impact of eddies on the response of the  
794 southern ocean to climate change. *Ocean Modelling*, **34** (34), 150 – 165, doi:<http://dx.doi.org/10.1016/j.ocemod.2010.05.005>, URL <http://www.sciencedirect.com/science/article/pii/S1463500310000806>.
- 797 Ward, M. L., and A. M. Hogg, 2011: Establishment of momentum balance by form stress in a  
798 wind-driven channel. *Ocean Modelling*, **40** (2), 133–146.

799 Wilson, C., C. W. Hughes, and J. R. Blundell, 2015: Forced and intrinsic variability in the re-  
800 sponse to increased wind stress of an idealized southern ocean. *Journal of Geophysical Re-*  
801 *search: Oceans*, **120** (1), 113–130, doi:10.1002/2014JC010315, URL <http://dx.doi.org/10.1002/2014JC010315>.  
802

<sup>803</sup> **LIST OF TABLES**

<sup>804</sup> **Table 1.** Table showing the different numerical experiments performed . . . . . 44

TABLE 1: Table showing the different numerical experiments performed

Forcing Period (years) ( $T$ )	Number Ensembles (M)	Number of years of integration per ensemble ( $N_T$ )	Sampling Frequency (days)	Number of Forcing cycles ( $\frac{N_T \times M}{T}$ )
1/4	4	15	2	240
1/2	4	25	5	200
1	4	50	5	200
2	8	50	5	200
4	8	100	10	200
8	8	200	20	200
16	8	400	40	200
Steady	4	50	5	—

## 805 LIST OF FIGURES

806	<b>Fig. 1.</b> Power Spectral density of the jet speed, jet latitude, wind stress and mean zonal wind over 807 the latitude region $35^{\circ}$ S - $70^{\circ}$ S for the (a) NCEP - NCAR reanalysis and (b) ERA - Interim 808 datasets with 6 hourly data. The power spectrum is computed using multi taper spectral 809 methods and has been smoothed with a 10 point smoothing Hanning window . . . . .	46
810	<b>Fig. 2.</b> The gain (left panel) and phase shift (right panel) of EKE and APE for the analytical model 811 of time dependent eddy compensation with no eddy feedback (equations 8 to 11) as a func- 812 tion of non-dimensionalised $\omega$ . . . . .	47
813	<b>Fig. 3.</b> The gain (top) and phase shift (bottom) of APE (left) and EKE (right) for the analytical 814 model of time dependent eddy compensation with the eddy feedbacks (equations 16 to 23) 815 as a function of non-dimensionalised $\omega$ (normalized by $c_1$ ) for different values of eddy 816 feedback rates ( $c_2$ ) drag coefficients ( $r$ ) . . . . .	48
817	<b>Fig. 4.</b> (a) Wind stress used for the numerical simulations with a steady part represented by the thick 818 black line and oscillating between the two thin lines with a frequency given by the forcing 819 frequency of the particular experiment. (b) The bottom topography used in the numerical 820 simulations showing meridionally symmetric gaussian ridge running down the middle of 821 the domain. (c) Snapshot of the model spinup showing the isopycnal layers and the relative 822 vorticity computed from the $u$ and $v$ fields for the top layer. . . . .	49
823	<b>Fig. 5.</b> Power Spectral density of Wind work input, Eddy Kinetic Energy, and Potential Energy for 824 the different forcing experiments . . . . .	50
825	<b>Fig. 6.</b> Power spectral density for the total zonal transport and the barotropic and baroclinic parts 826 for the different experiments . . . . .	51
827	<b>Fig. 7.</b> Amplitude of oscillation for EKE, PE and KE, computed from the psd's EKE, KE and PE, 828 normalized with the maximum amplitude of the wind work for each of the variable wind 829 forcing experiments as a function of the forcing frequency . . . . .	52
830	<b>Fig. 8.</b> Schematic describing the method used for calculating the composite of a particular variable 831 for the composite analysis . . . . .	53
832	<b>Fig. 9.</b> Composites of EKE, PE and wind energy input calculated over all ensemble members and all 833 forcing cycles plotted as periodic signals with period corresponding to the external forcing 834 frequency . . . . .	54
835	<b>Fig. 10.</b> Composites of barotropic and baroclinic zonal transport calculated over all ensemble mem- 836 bers and all forcing cycles plotted as periodic signals with period corresponding to the ex- 837 ternal forcing frequency. Both of these quantites are shown about a zero mean. . . . .	55
838	<b>Fig. 11.</b> (a) R.m.s Amplitude of oscillations of EKE and PE normalized by the r.m.s. amplitude 839 of wind power plotted as a function of the forcing period shown alongside the standard 840 deviation ("noise floor") in each of these quantites (dashed lines) for the different ensemble 841 experiments (b) phase shift of each of the quantites (PE, EKE, mean kinetic energy and zonal 842 transport) as a function of the forcing period with the standard deviation shown by shading . . . . .	56
843	<b>Fig. 12.</b> Amplitude and phase of EKE and PE calculated for the 2 analytic cases: Partial eddy sat- 844 uration (blue) and total eddy saturation (green) with quadratic drag compared with the values 845 calculated from the numerical model (black). . . . .	57

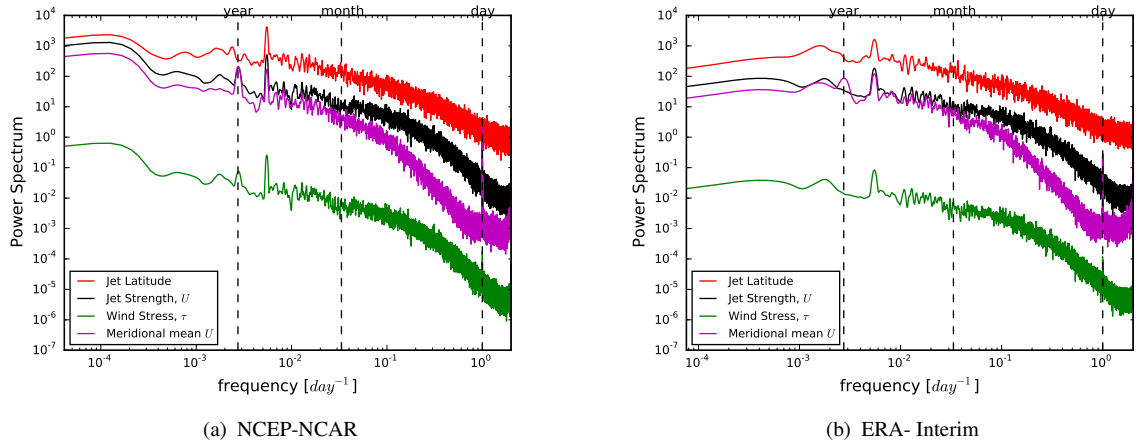


FIG. 1: Power Spectral density of the jet speed, jet latitude, wind stress and mean zonal wind over the latitude region  $35^\circ$  S -  $70^\circ$  S for the (a) NCEP - NCAR reanalysis and (b) ERA - Interim datasets with 6 hourly data. The power spectrum is computed using multi taper spectral methods and has been smoothed with a 10 point smoothing Hanning window

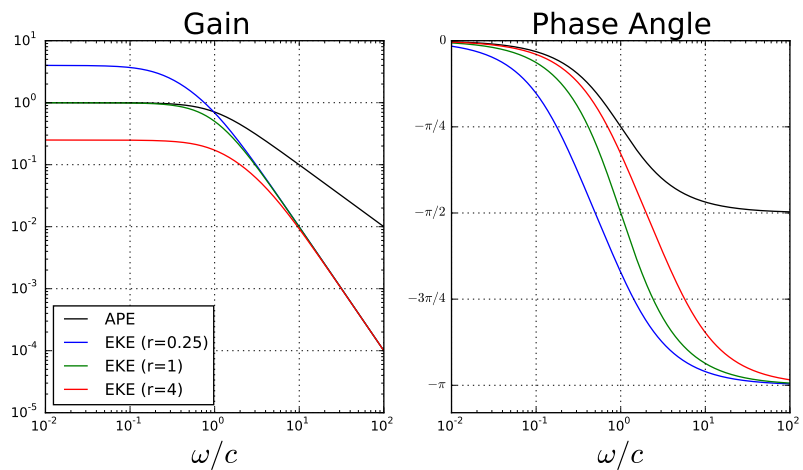


FIG. 2: The gain (left panel) and phase shift (right panel) of EKE and APE for the analytical model of time dependent eddy compensation with no eddy feedback (equations 8 to 11) as a function of non-dimensionalised  $\omega$ .

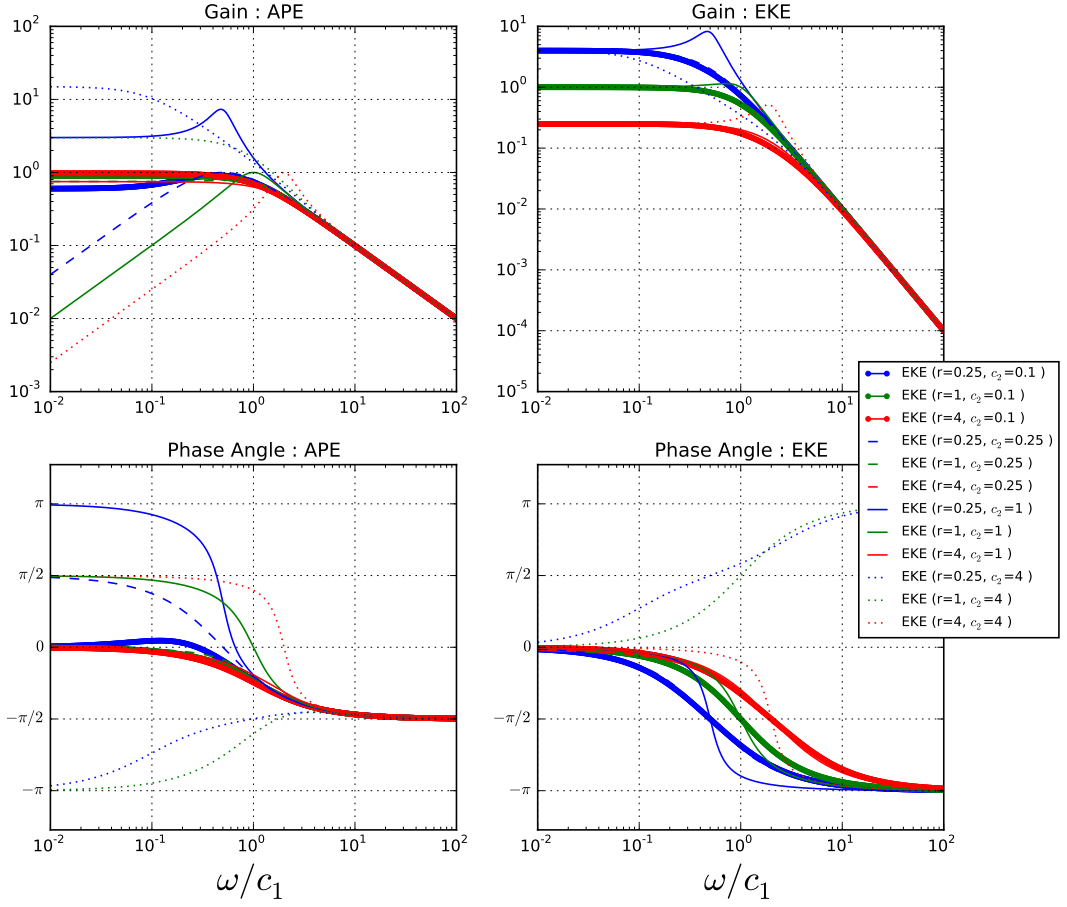
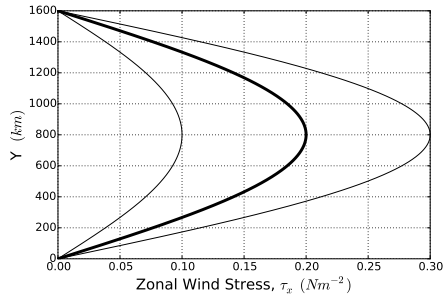
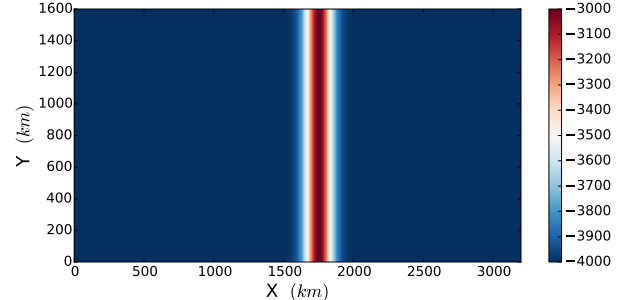


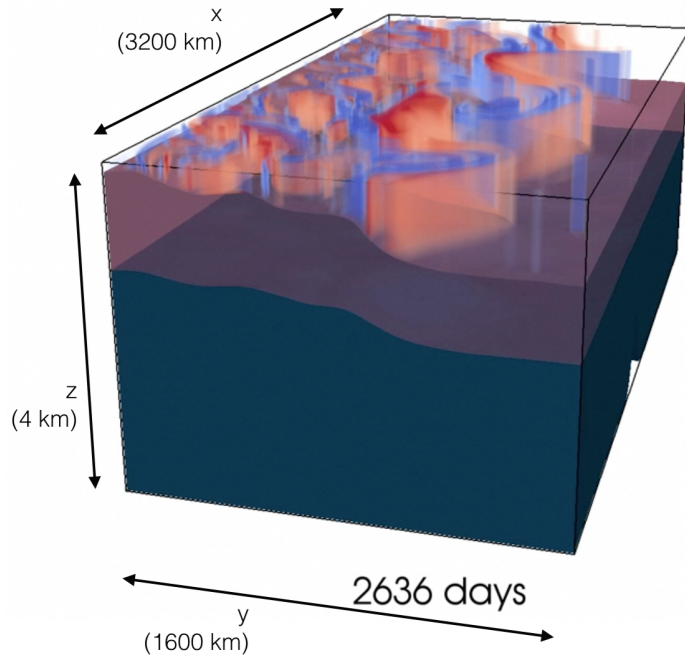
FIG. 3: The gain (top) and phase shift (bottom) of APE (left) and EKE (right) for the analytical model of time dependent eddy compensation with the eddy feedbacks (equations 16 to 23) as a function of non-dimensionalised  $\omega$  (normalized by  $c_1$ ) for different values of eddy feedback rates ( $c_2$ ) drag coefficients ( $r$ ).



(a) wind stress



(b) bottom topography



(c) snapshot of model spinup

FIG. 4: (a) Wind stress used for the numerical simulations with a steady part represented by the thick black line and oscillating between the two thin lines with a frequency given by the forcing frequency of the particular experiment. (b) The bottom topography used in the numerical simulations showing meridionally symmetric gaussian ridge running down the middle of the domain. (c) Snapshot of the model spinup showing the isopycnal layers and the relative vorticity computed from the  $u$  and  $v$  fields for the top layer.

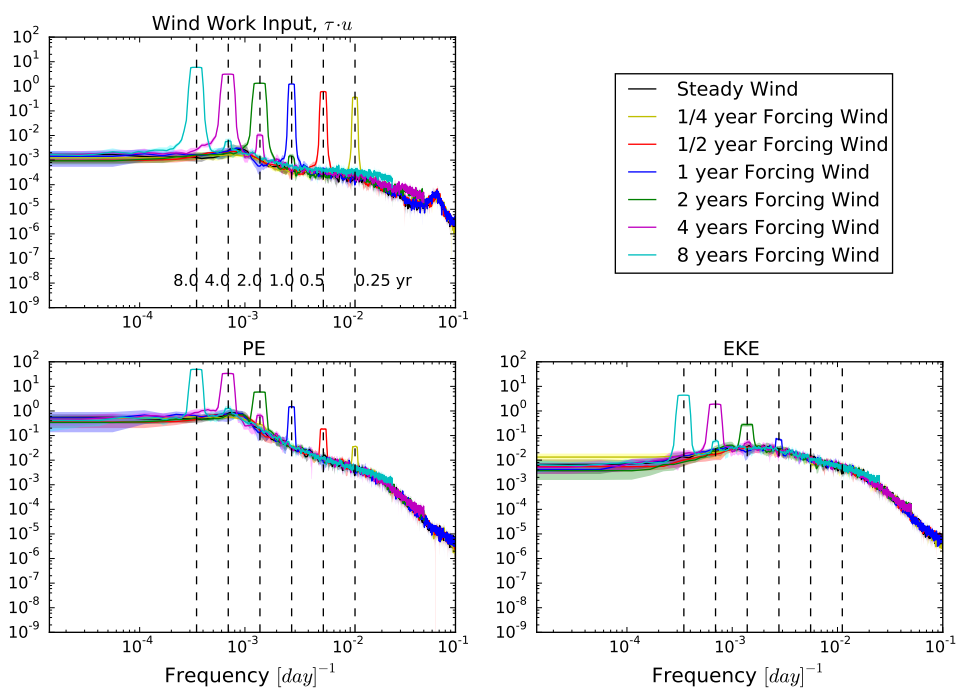


FIG. 5: Power Spectral density of Wind work input, Eddy Kinetic Energy, and Potential Energy for the different forcing experiments.

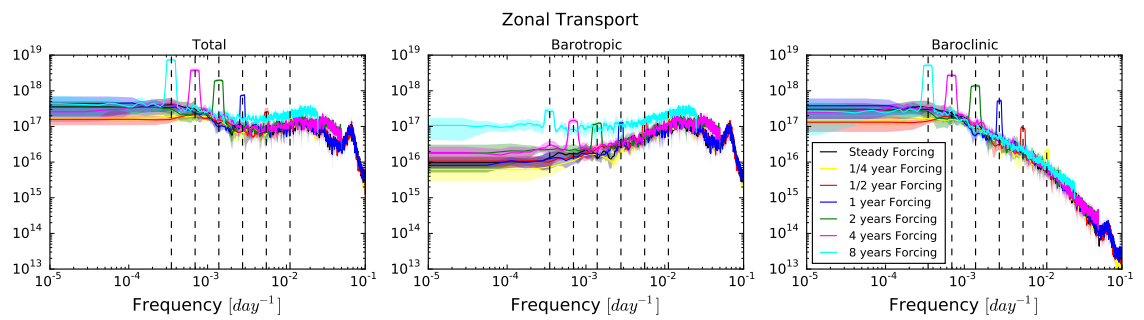


FIG. 6: Power spectral density for the total zonal transport and the barotropic and baroclinic parts for the different experiments

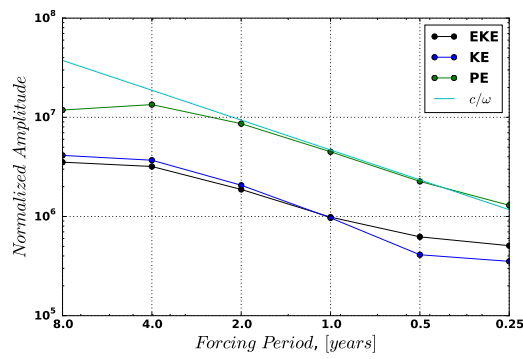


FIG. 7: Amplitude of oscillation for EKE, PE and KE, computed from the psd's EKE, KE and PE, normalized with the maximum amplitude of the wind work for each of the variable wind forcing experiments as a function of the forcing frequency.

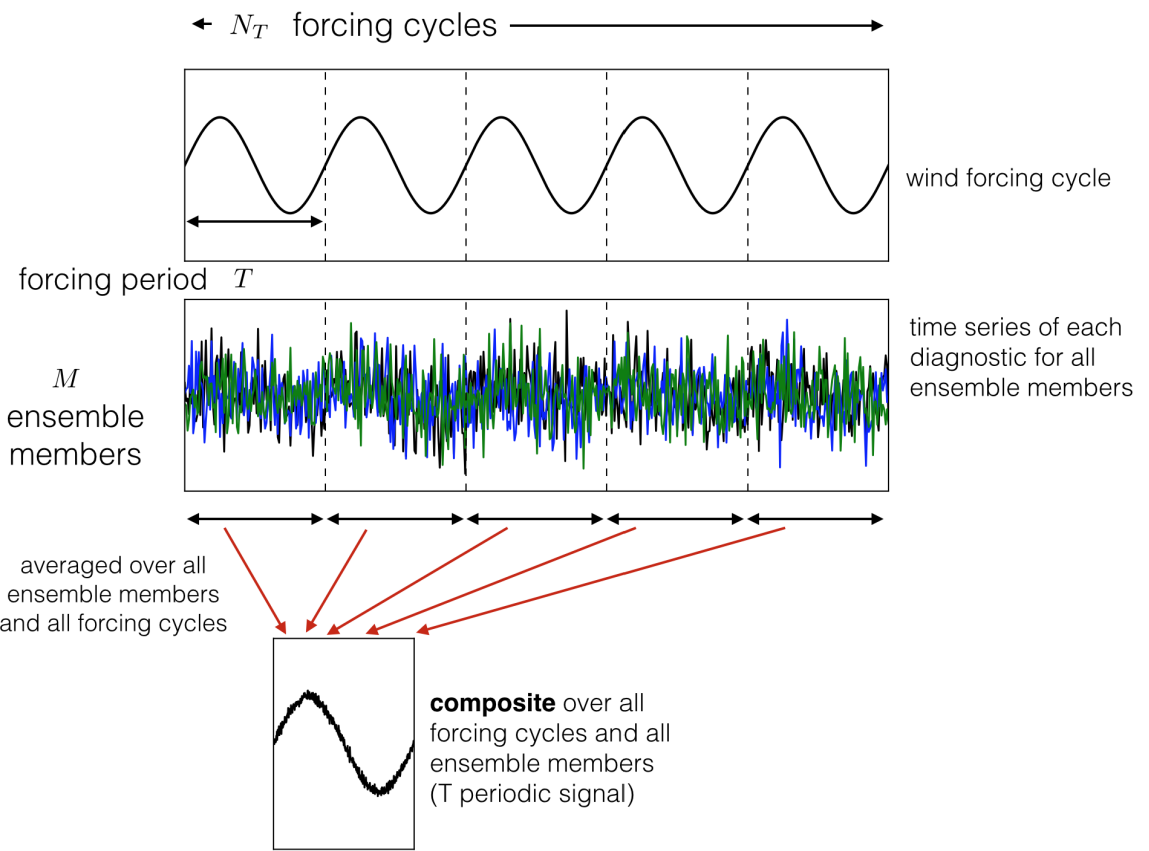


FIG. 8: Schematic describing the method used for calculating the composite of a particular variable for the composite analysis

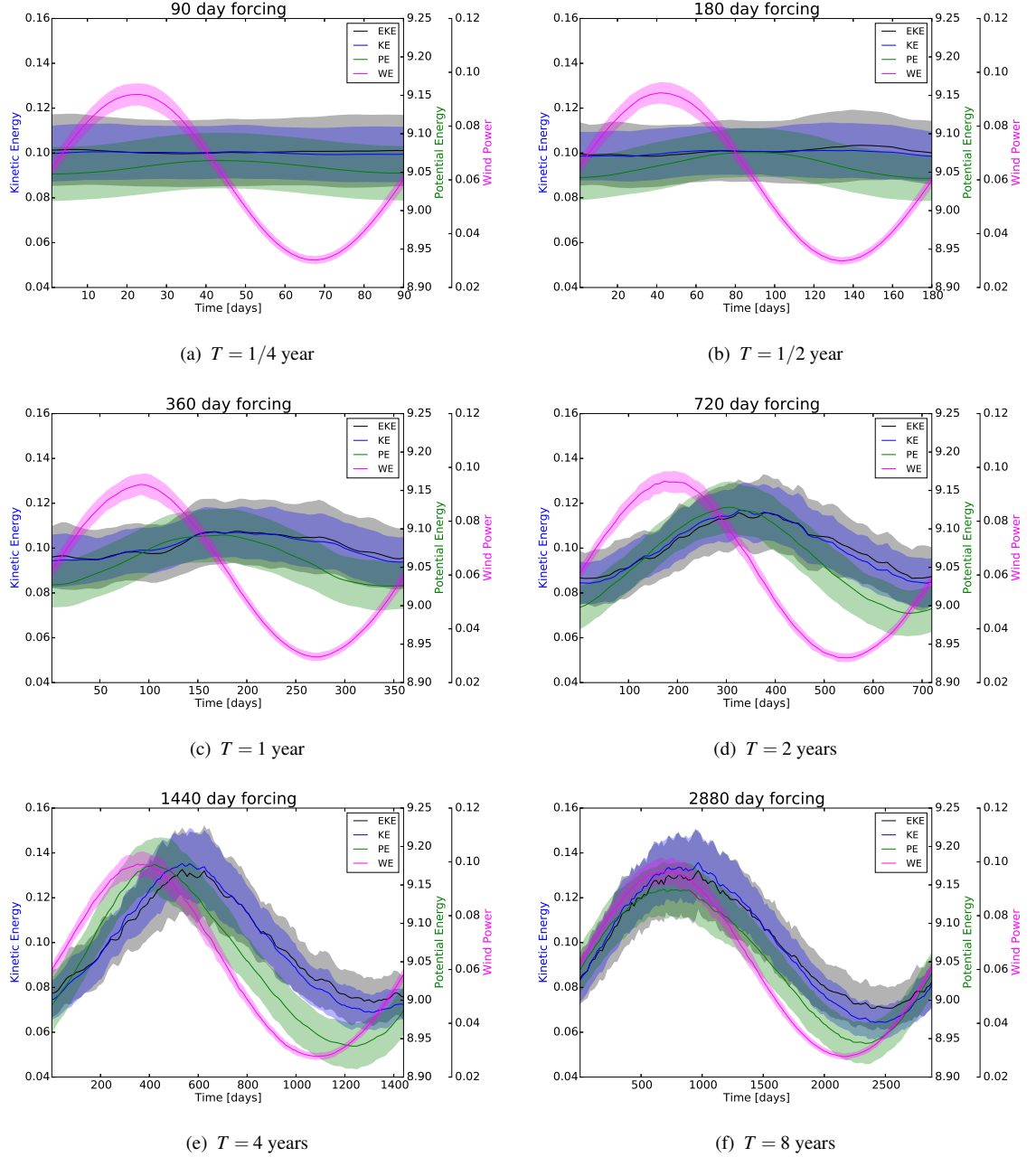


FIG. 9: Composites of EKE, PE and wind energy input calculated over all ensemble members and all forcing cycles plotted as periodic signals with period corresponding to the external forcing frequency.

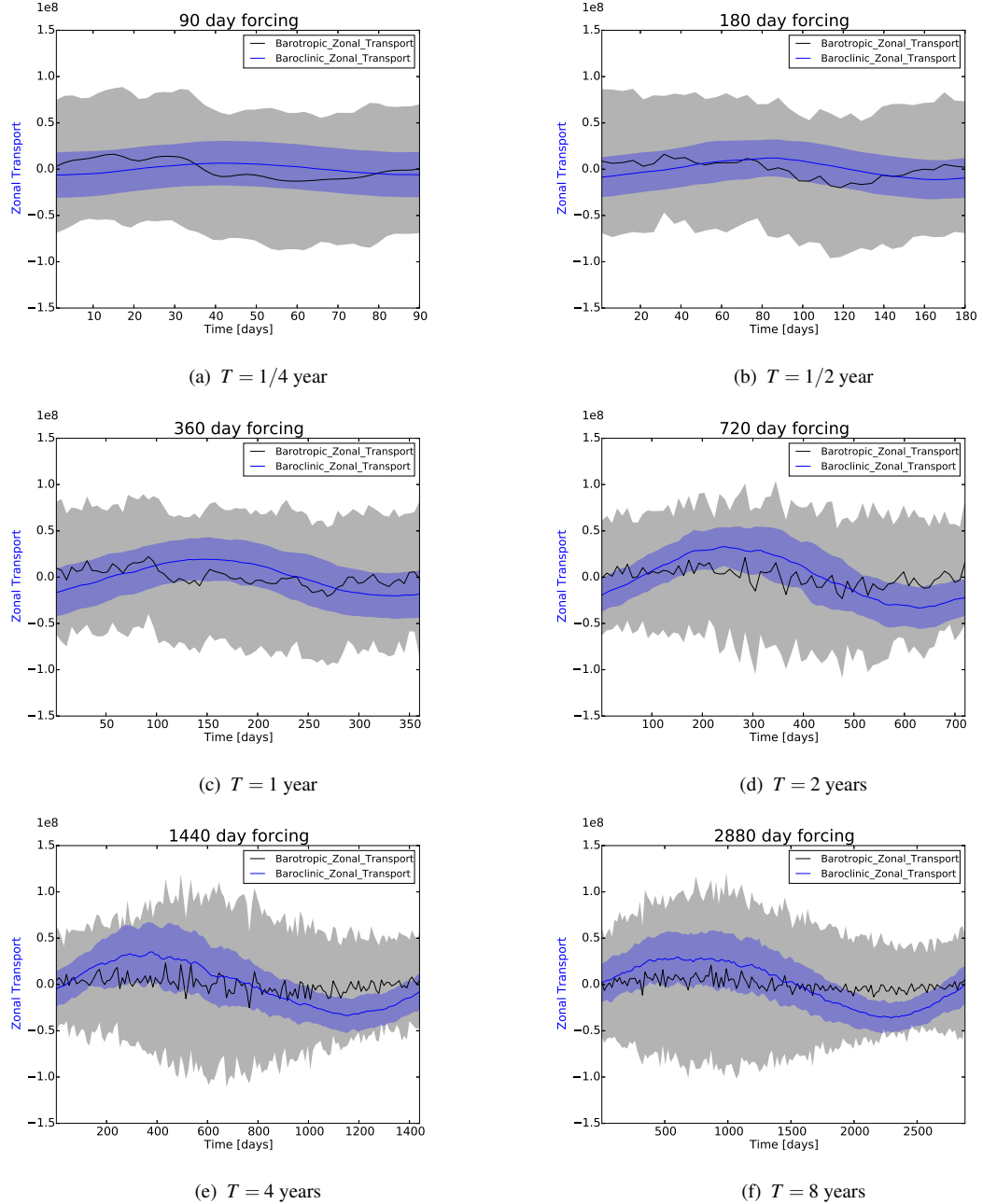


FIG. 10: Composites of barotropic and baroclinic zonal transport calculated over all ensemble members and all forcing cycles plotted as periodic signals with period corresponding to the external forcing frequency. Both of these quantities are shown about a zero mean.

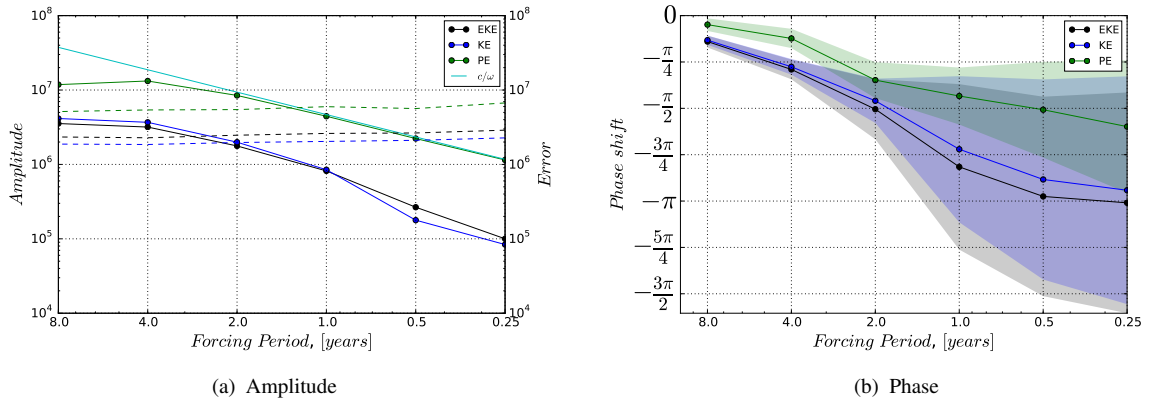


FIG. 11: (a) R.m.s Amplitude of oscillations of EKE and PE normalized by the r.m.s. amplitude of wind power plotted as a function of the forcing period shown alongside the standard deviation (“noise floor”) in each of these quantites (dashed lines) for the different ensemble experiments (b) phase shift of each of the quantites (PE, EKE, mean kinetic energy and zonal transport) as a function of the forcing period with the standard deviation shown by shading.

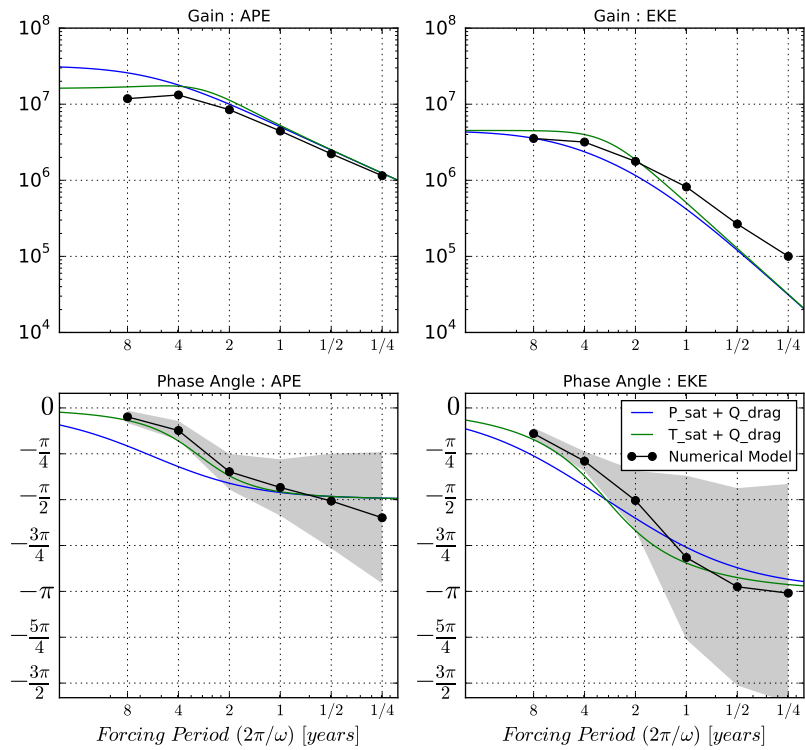


FIG. 12: Amplitude and phase of EKE and PE calculated for the 2 analytic cases: Partial eddy saturation (blue) and total eddy saturation (green) with quadratic drag compared with the values calculated from the numerical model (black).